Chemical Geology 509 (2019) 163–177

Contents lists available at ScienceDirect

Chemical Geology

journal homepage: www.elsevier.com/locate/chemgeo

Modern carbonate ooids preserve ambient aqueous REE signatures

Fei Li[a,b,*], Gregory E. Webb[b], Thomas J. Algeo[c,d,e], Stephen Kershaw[f], Chaojin Lu[g,h], Amanda M. Oehlert[h], Qiaolin Gong[a], Ali Pourmand[h], Xiucheng Tan[a,i]

[a] State Key Laboratory of Oil and Gas Reservoir Geology and Exploitation, Southwest Petroleum University, Chengdu 610500, China
[b] School of Earth and Environmental Sciences, The University of Queensland, Brisbane, QLD 4072, Australia
[c] State Key Laboratory of Biogeology and Environmental Geology and School of Earth Sciences, China University of Geosciences, Wuhan 430074, China
[d] State Key Laboratory of Geological Processes and Mineral Resources, China University of Geosciences, Wuhan 430074, China
[e] Department of Geology, University of Cincinnati, Cincinnati, OH 45221-0013, USA
[f] Institute for the Environment, Brunel University, Uxbridge UB8 3PH, UK
[g] College of Geosciences, China University of Petroleum (Beijing), Beijing 102249, China
[h] Department of Marine Geosciences, Rosenstiel School of Marine and Atmospheric Science, University of Miami, Miami, FL 33149, USA
[i] Division of Key Laboratory of Carbonate Reservoirs of CNPC, Southwest Petroleum University, Chengdu 610500, China

ARTICLE INFO

Editor: Balz Kamber

Keywords:
Rare earth elements
Ce anomaly
LA-ICP-MS
Great Bahama Bank
Great Salt Lake
Carbonate REE + Y compositions

ABSTRACT

Skeletal and non-skeletal components of marine sedimentary rocks have been analyzed for the purpose of reconstructing the rare earth element (REE) and yttrium (Y) compositions of paleo-seawater, but skeletal carbonates frequently have proven to be unreliable recorders of seawater chemistry. Here, we present a systematic multi-technique assessment of rare earth and other trace elements in ooid sands from the modern Great Bahama Bank (GBB–marine) and Great Salt Lake (GSL–continental) based on strong-acid (hydrofluoric and nitric) and weak-acid (acetic) digestions, as well as laser ablation (LA) of ooid cortices and nuclei. The results show that Bahamian ooid cortices possess shale-normalized REE + Y features nearly identical to those of shallow seawater, including limited contamination from siliciclastic REEs. An admixture of even 0.2% of detritally sourced material can modify the primary marine REE + Y patterns by, for example, increasing the light REE (LREE) content. Mean values of LA data for Bahamian ooid cortices exhibit similar REE + Y signatures to those produced by acetic acid digestion, but LA data are generally noisier, primarily as a result of low REE concentrations and the small volume of carbonate ablated in analysis. Screening out samples with ΣREE < 0.9 ppm reveals more uniform, seawater-like REE + Y patterns in individual ooid cortices as well as high, uniform REE distribution coefficients (116 ± 21, from La to Lu) with respect to ambient seawater. Ooid laminae show no distinct alternation between oxic and anoxic pore fluid characteristics, suggesting that growing ooids primarily formed under oxic conditions in carbonate shoal settings, even when buried during their resting phase. Unlike Bahamian ooids, shale-normalized REE + Y patterns of GSL ooids digested in weak acid show slightly depleted LREE compositions that may deviate from ambient fluids owing to release of REEs from an included clay fraction based on comparison between digestion and LA methods. Multiple ablation spots within the same cortex allowed direct comparison of more and less contaminated portions of a single ooid. Nearly uniform positive Ce anomalies may be related to strongly alkaline water conditions. Individual ablation spots that are partially overprinted by siliciclastic-derived REEs contain variable Zr contents (from 0.096 to ~4 ppm) and flattened shale-normalized LREE patterns. The least-contaminated GSL ooid cortex yields an LREE-depleted REE + Y distribution. Normalization of the REE + Y distributions of least-contaminated GSL ooids using reliable GBB ooid distributions (i.e., with ΣREE > 0.9 ppm) returns a flat pattern, suggesting similar degrees of LREE depletion controlled by carbonate complexation under similar aqueous alkalinity conditions in Great Salt Lake and Bahamian waters. In summary, ooids can be a reliable proxy for REE + Y characteristics of ambient surficial waters when adopting suitable analytical methods, including laser ablation, that allow the identification and isolation of a contamination signal from siliciclastic detritus.

* Corresponding author at: State Key Laboratory of Oil and Gas Reservoir Geology and Exploitation, Southwest Petroleum University, Chengdu 610500, China.
E-mail address: feinan.li@gmail.com (F. Li).

https://doi.org/10.1016/j.chemgeo.2019.01.015
Received 21 September 2018; Received in revised form 18 January 2019; Accepted 25 January 2019
Available online 01 February 2019
0009-2541/ © 2019 The Authors. Published by Elsevier B.V. This is an open access article under the CC BY license (http://creativecommons.org/licenses/BY/4.0/).

1. Introduction

Aqueous rare earth element (REE) and yttrium (Y) distributions can provide useful information to identify, differentiate, and trace different watermasses (Piper, 1974; Elderfield et al., 1990). The main sources of REE + Y to seawater are terrigenous (e.g., riverine and aeolian) and seafloor (e.g., hydrothermal and porewater) fluxes (Henderson, 1984; Elderfield and Sholkovitz, 1987; Bayon et al., 2004). The REE + Y distribution of seawater is the product of a series of biochemical reactions and partitioning effects that are mostly related to adsorption/desorption onto colloids in the water column and various mineral phases in the sediment (Henderson, 1984; Sholkovitz et al., 1994).

Modern REE + Y compositions of oxic seawater are generally characterized by enrichment of heavy REEs (HREE, from Ho to Lu) relative to light REEs (LREE, from La to Nd) on a shale-normalized basis, superchondritic ratios of Y/Ho, and negative Ce and positive La anomalies. HREE enrichment is due primarily to an increase in the degree of carbonate complexation from La^{3+} (z = 57) to Lu^{3+} (z = 71) (Nozaki, 2001). Owing to differences in their complexation behavior, Ho is scavenged by particles at roughly twice the rate of Y, leading to superchondritic Y/Ho ratios (~44–74) in seawater (Nozaki et al., 1997). A negative Ce anomaly can develop through depletion of Ce^{3+} in aqueous systems due to its oxidation to Ce^{4+} on the surfaces of suspended particles (e.g., Mn oxides) (Ohta and Kawabe, 2001) or to microbial scavenging processes combined with quick removal to the sediment (Moffett, 1990; Sholkovitz et al., 1994). A positive La anomaly can develop owing to its higher stability (empty 4f electron shell) relative to neighboring REEs (de Baar et al., 1985). Some alkaline river and lake waters support similar carbonate-complexation processes and can exhibit more-or-less similar REE characteristics and behaviors to seawater (Möller and Bau, 1993; Shiller, 2002).

Modern seawater REE + Y concentrations can be measured directly from filtered waters, but the REE composition of paleo-seawater is more difficult to determine. Numerous sedimentary components of both biotic (e.g., calcareous/phosphatic bioclasts) and abiotic origin (e.g., primary and authigenic minerals) have been tested to evaluate their REE characteristics against modern seawater. Many biological proxies consisting of unburied, clean material (e.g., corals (Scherer and Seitz, 1980; Sholkovitz and Shen, 1995), articulated brachiopods (Zaky et al., 2016a), and foraminifera (Palmer, 1985; Osborne et al., 2017)) yield seawater-like REE + Y distributions, although biological fractionation effects have been reported (Akagi et al., 2004; Saha et al., 2016; Zaky et al., 2016a). However, buried fossils commonly lose their original signatures due to secondary uptake of REEs from porewaters during shallow-burial diagenesis, especially when exposed to REEs from non-carbonate sources (Haley et al., 2004; Abbott et al., 2015; Chen et al., 2015). For these reasons, shallow-water non-skeletal proxies with minimum exposure to siliciclastic particles and limited burial fluids, e.g., reefal microbialites (Webb and Kamber, 2000) and early cements (Nothdurft et al., 2004; Wallace et al., 2017), generally yield seawater-like REE distributions and uniform distribution coefficients (D, except for Ce) (D of microbialites from Webb and Kamber, 2000; D of cements calculated from Wallace et al., 2017). These components have been used widely to evaluate paleo-seawater REE compositions (e.g., Della Porta et al., 2015; Wallace et al., 2017; Hood et al., 2018).

Recently, Li et al. (2017) showed that Lower Triassic ooids yield modern seawater-like REE signatures, thus suggesting the general utility of ooids for assessment of paleo-seawater compositions. Other studies have documented the REE compositions of ancient oolitic sediments but generally have not compared them with modern seawater REE characteristics (Siahi et al., 2017; Wallace et al., 2017; de Paula-Santos et al., 2018; Kalvoda et al., 2018). Uncertainties exist owing to the limited information about secular changes in seawater REE + Y through time (e.g., Shields and Webb, 2004) and possible contamination of REE + Y signatures by minor siliciclastic fractions in analyzed sediments.

In view of the potential of ooids for analysis of seawater REE + Y signatures through time, the present study was designed to establish a 'baseline' with regard to modern ooid chemistry. Here, we analyze the REE + Y compositions of modern ooids from different depositional settings, i.e., marine ooids from the Great Bahama Bank (GBB; Bahamas) and lacustrine ooids from the Great Salt Lake (GSL; Utah, western USA). To achieve the most robust results possible, we make use of multiple analytical techniques, including three different dissolution protocols (i.e., strong-acid digestions of bulk ooids and non-carbonate fractions, and weak-acid digestion of carbonate fractions) as well as in situ laser ablation inductively coupled plasma-mass spectrometry (LA-ICP-MS). We investigated the REE + Y signatures of ooids having various internal microstructures, contamination sources, and original aqueous chemical conditions. This study thus provides insights into the efficacy of multiple analytical techniques for analysis of ooid REE + Y compositions, various environmental influences thereon, and constraints for interpretation of paleo-seawater REE + Y chemistry.

2. Sample sources and background

2.1. Bahamian ooids

Marine ooid sands were collected from tidal flat settings (< 5 m in depth) at Joulter Cays and Schooner Cays on the Great Bahama Bank (GBB). The sampling site at Joulter Cays is an exposed windward shoal located at the northern end of Andros Island (GPS: 25°17′22.7″ N, 78°07′13.0″ W). The sampling site at Schooner Cays is situated on a protected leeward beach on southwestern Eleuthera Island (GPS: 24°57′1.6″ N, 76°24′9.1″ W), although it lies near the southern end of the deep Exuma Sound embayment where rapid tidal currents (2 m/s) are common (Bergman et al., 2010). The Bahamian ooid sands are nearly pure carbonate (99.2% by volume), with aragonite (91.6%) dominant over high-Mg calcite (7.5%; mainly derived from certain skeletal fragments) (Reijmer et al., 2001; Swart et al., 2014). Seawater alkalinity (as measured at Joulter Cays and Eleuthera) is 6.50 to 9.62 meq/L, and pH ranges from 8.55 to 8.75 in the leachates of ooid sands (Diaz et al., 2015). Sands from both sites are composed of well-sorted, carbonate ooids with mean diameters of 0.3 ± 0.1 mm (reported with ± 1σ standard deviation; n = 103) at Joulter Cays and 0.9 ± 0.3 mm (n = 418) at Schooner Cays. The study samples have no more than 5% (by volume; based on microscopic point counts) of pellets and fossil fragments (e.g., foraminifers, calcareous algae). These non-ooid components together with grapestone lumps generally act as nuclei and occupy ~39% of total ooid area in microscopic view (based on point counting; grid range 50 μm × 50 μm; ooid number (n) = 126) (method from Flügel, 2004). Ooid cortices typically consist of tangentially oriented fabrics, and no more than 2% of ooids contain apparent micritic structures. Morphological characteristics of these GBB ooid sands are shown in Fig. S1.

2.2. Great Salt Lake ooids

The Great Salt Lake (GSL), a remnant of the larger ancient Lake Bonneville, is one of the largest closed lake basins (i.e., lacking a river outlet) in the modern world. It is known for its high alkalinity (~7 meq/L at 0–5 m water depth, and pH = 8.6 at 25 °C), hypersalinity (50.4–263 g/L), and Na-Mg-Cl-SO_4 brine compositions (Domagalski et al., 1990; Jones et al., 2009; Chagas et al., 2016). Today, the GSL is

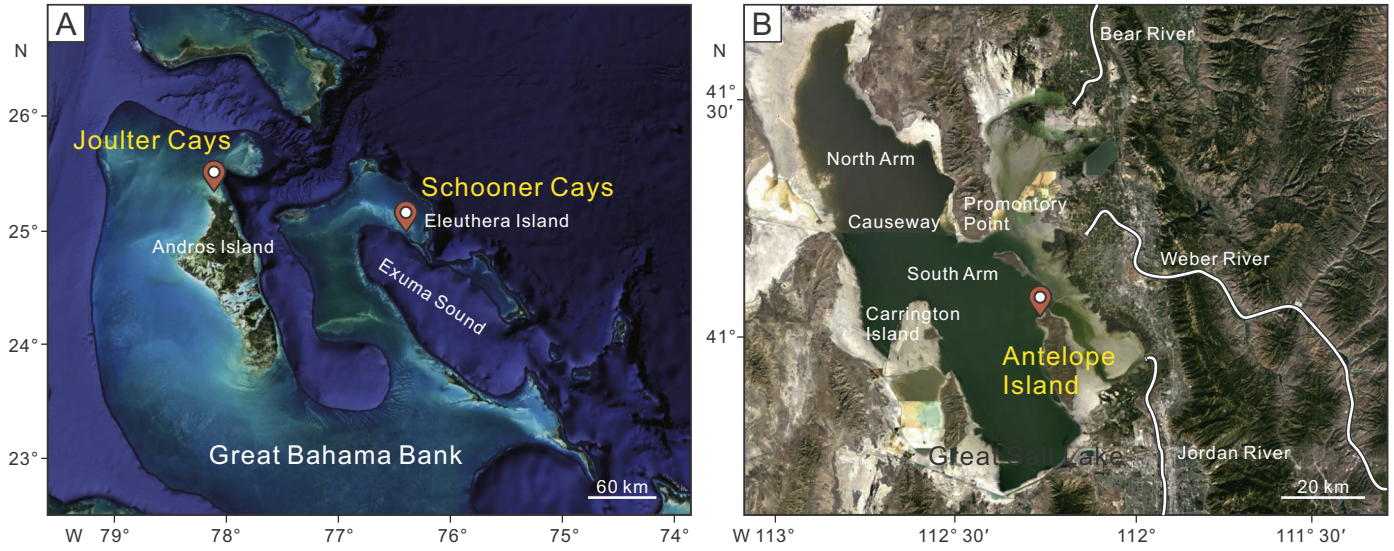

Fig. 1. Satellite imagery of study areas and sampling localities (marked) on the Great Bahama Bank and the Great Salt Lake. Images from Google Earth.

separated into northern and southern arms by a causeway formed of cemented carbonates (Fig. 1B). The southern part contains a subaqueous carbonate ridge extending roughly from Carrington Island to Promontory Point, and receives more surface runoff than the northern arm (Fig. 1B; Spencer et al., 1984). The sampling site is situated nearshore (at < 4 m water depth) on the northern side of Antelope Island (GPS: 41°2′40.0″ N, 112°16′1.5″ W), South Arm (Fig. 1B). The ooid sands are composed of carbonate (> 90% aragonite), with some admixture of siliciclastic grains (mostly quartz, and a few feldspars) and pellets, clay minerals, and rare heavy mineral grains (Halley, 1977). Ooid nuclei include both non-carbonate (e.g., quartz, feldspar, lithic fragments) and a few carbonate grains (e.g., fecal pellets), and they occupy ~19% of total ooid area in microscopic view based on the same method as used for the Bahamian ooids (n = 231). Although the main mineralogy of GSL ooid cortices (aragonite) is the same as for the GBB, GSL ooids exhibit a greater variety of cortical fabrics than the uniformly tangential fabrics of GBB ooids, including radial, tangential, radial-concentric, mixed radial and concentric (with inner radial and outer concentric, as well as alternately radial and concentric crystallite orientations), and micritic fabrics (Fig. S1).

3. Methods

To better distinguish differences in the trace and rare earth element contents of bulk ooid sands, ooid carbonate, siliciclastic components, and individual ooid cortices, four different sample processing workflows were utilized (Fig. S2). Processing flow A (PFA) used strong acids (hydrofluoric and nitric) to achieve complete dissolution of bulk ooid sands (i.e., carbonate plus non-carbonate components). The carbonate and non-carbonate fractions of the bulk samples were separated through processing flows B and C. PFB used a weak acid (acetic) to dissolve the carbonate fraction of ooids, and the residue from PFB was then fully dissolved in strong acids (hydrofluoric and nitric) to recover the non-carbonate fraction of ooids (PFC). Processing flow D (PFD) utilized LA-ICP-MS to measure the composition of small features within individual ooids (e.g., cortical laminae and nuclei).

3.1. Solution-ICP-MS analysis of bulk ooid sands (strong-acid-digestion; PFA)

Bulk samples of GBB and GSL ooid sands were ground in an agate mill to powder finer than 200 mesh, and then placed in an oven at 40 °C to dry for 12 h. The following procedures were then applied: (A1) weigh out 50 mg powder and dissolve in 1 mL of HNO_3 and 1 mL of HF; (A2) place the solution on a hotplate (ca. 140 °C) and evaporate to incipient dryness, and then repeat this dry-down process after adding 1 mL HNO_3; (A3) complete dissolution of residue in 1 mL of HNO_3, 1 mL of Milli-Q water, and 1 mL internal standard solution (Table S1); and (A4) dilute to 100 g solution via adding 1% HNO_3 for analysis using ICP-MS for bulk sediment compositions.

3.2. Solution-ICP-MS analyses of carbonate (weak-acid-digestion; PFB) and non-carbonate (strong-acid-digestion; PFC) fractions of ooid sands

Two processing flows were carried out in order to separate the carbonate (PFB) and non-carbonate (PFC) fractions of the bulk samples. PFB followed this protocol: (B1) weigh out 500 mg of powdered sample and dissolve in 30 mL CH_3COOH (1 M acetic acid) at room temperature for ca. 24 h; (B2) centrifuge the solution and separately collect the supernatant and insoluble material; (B3) place the supernatant on a hotplate (ca. 105 °C) for 12 h until all CH_3COOH is volatilized; (B4) complete dissolution of residue in 1 mL of HNO_3, 1 mL of Milli-Q water, and 1 mL internal standard solution (same protocol as step A3 of PFA, as above), and then (B5) dilute to 50 mL solution via addition of 1% HNO_3 for ICP-MS analysis of the carbonate-sourced fraction.

The PFC flow utilizes the centrifuged insoluble CH_3COOH-leached concentrate from step B2 and then: (C1) weigh out 50 mg of insoluble residue and dissolve in 1 mL of HNO_3 and 1 mL of HF; and (C2) carry out same protocol as steps A2 to A4 of PFA (as above) to acquire data for the non-carbonate fraction. Because the mean $CaCO_3$ content of GBB ooids is > 99% (see Section 2.1), almost the entirety of each sample was dissolved in acetic acid and, consequently, analysis of the insoluble fraction was not possible for those ooids owing to insufficient material. The technique was applied successfully to the GSL sample.

The sample digestion protocols (PFA, PFB and PFC) were performed at two different laboratories for the purpose of data comparison: (1) at the Life Sciences & Chemical Analysis Laboratory of Agilent Technologies Inc. in Chengdu (Agilent 7700x ICP-MS), and (2) at Thermo Fisher Scientific Inc. in Shanghai (iCAP RQ ICP-MS). A suite of trace and rare earth elements consisting of Al, Sc, Zr, Y, La, Ce, Pr, Nd, Sm, Eu, Gd, Tb, Dy, Ho, Er, Tm, Yb, Lu, and Th were analyzed in this study. Aluminum was investigated in GSL ooids only for flow PFB in order to check Al concentrations of the carbonate fraction. Each sample was calculated as a mean value from two duplicate measurements on

the same solution with relative error < 5%. Results were calibrated with internal standards and standard solutions provided by each laboratory. Oxide interferences (e.g., BaO on Eu), although weak, were monitored during each analytical session (for working parameters see Table S1).

3.3. In situ LA-ICP-MS analysis of ooid cortices and nuclei (PFD)

Ooid-sand samples were embedded in epoxy resin and made into thin sections for LA-ICP-MS analysis. Each pre-set position for laser ablation analysis was determined under a polarized- and reflected-light microscope to locate the ooid/cortex (marked with ink) and locations were chosen to avoid visible boring traces, breaks, and siliciclastic grains (Fig. S1). Ooid cortical REE + Y compositions were calculated from the mean value of spots in each ooid (generally five spots). Thin sections were washed and sonicated in beakers of ultrapure water prior to analysis. Analyses were measured using an integrated in situ laser ablation (COMPexPro 102 ArF 193 nm excimer laser; Coherent GeoLasPro) and ICP-MS (Agilent 7700e) system at the Sample-Solution Analytical Technology Co. in Wuhan, China. Internal standard-independent calibrations followed the procedure of Chen et al. (2011). One test sequence included 50 sample spots and within each five-spot measurement was inserted one analysis of NIST 610 for drift correction, while a series of standard materials were measured before (NIST610, BHVO-2G, BIR-1G, BCR-2G, MACS-3, and MACS-3 in order) and after (MACS-3, MACS-3, BCR-2G, BIR-1G, BHVO-2G, and NIST610 in turn) the run to set a calibration curve. Each spot analysis incorporated an initial < 5 s wash-out time then ~20 s background acquisition, followed by a ~50 s sample-data acquisition interval. The laser-spot size of 44 μm was reliable in light of large quantities of repeated measurements (n = 308) on reference carbonate material MACS-3 from United States Geological Survey (USGS) during this study, and the relative deviations of REE + Y concentrations were < 7% (Table S2). A smaller laser-spot size (< 44 μm) tends to increase analytical instability (Chen et al., 2011) and thus was not attempted. The measured isotopes of REE + Y include ^{89}Y, ^{139}La, ^{140}Ce, ^{141}Pr, ^{146}Nd, ^{147}Sm, ^{153}Eu, ^{157}Gd, ^{159}Tb, ^{163}Dy, ^{165}Ho, ^{166}Er, ^{169}Tm, ^{172}Yb, and ^{175}Lu. Some other elemental contents (^{27}Al, ^{45}Sc,^{49}Ti, ^{55}Mn, ^{57}Fe, ^{88}Sr, ^{91}Zr, and ^{232}Th) were also measured to test for possible contaminants, including the ink used to mark the thin sections, and/or early diagenetic signatures within ooid grains; their relative deviations were < 6% except for Al (< 9%) (see Table S2). ICPMSDataCal (version 10.7) software was used to calculate and calibrate off-line data (Liu et al., 2008). The signal intensities on paired elements (Al and Zr) were monitored spot-by-spot (reported as raw counts per second) to avoid possible inclusion of contaminants. Comparison of individual spot analyses showed that the ink used to locate the ablation spot did not affect measurements of elements of interest (e.g., Webb and Kamber, 2011). The instrument parameters (e.g., laser energy) and reference material could not effectively calibrate quartz and feldspar, and thus the concentrations of trace and rare earth elements of these types of ooid nuclei were not obtained in this study.

Additionally, five LA spots (50 μm diam.) were analyzed on ooid nucleus at Schooner Cays with extremely low REE concentrations by a combined ASI RESOlution SE laser ablation (ArF 193 nm gas excimer laser) and Thermo Fisher iCAP RQ ICP-MS system at the Radiogenic Isotope Facility, University of Queensland. The standards NIST 612 and 614 were used to correct for drift and check measurement uncertainties (five spots, Ca as internal standard; relative REE + Y concentration errors < 5%), respectively. Data processing and calibration was performed in Iolite (method from Paton et al., 2011).

Raw REE + Y concentrations were normalized to Post-Archean Australian Shale (PAAS) (McLennan, 1989) for comparison to seawater, and all reported REE values are shale-normalized unless otherwise indicated. Promethium (Pm, z = 61) is not naturally occurring and is represented by a space between Nd and Sm in REE distributions, and yttrium (Y, z = 39) was inserted between Dy and Ho to correctly order it on the basis of effective ionic radius (Bau and Dulski, 1996). The ratios of $(Pr/Yb)_{SN}$, $(Pr/Tb)_{SN}$, and $(Tb/Yb)_{SN}$ were used to evaluate relative enrichments of the LREE, MREE (from Sm to Dy), and HREE fractions. Some strong anomalies in Yb_{SN} (PFB results of GSL ooids) may affect the evolution of LREE depletion, and were replaced with the mean value of neighboring Tm_{SN} and Lu_{SN}. $(La/La^*)_{SN}$, $(Ce/Ce^*)_{SN}$, $(Eu/Eu^*)_{SN}$, $(Gd/Gd^*)_{SN}$, and $(Y/Y^*)_{SN}$ represent La, Ce, Eu, Gd, and Y anomalies that were calculated geometrically as follows (Y anomaly from Shields and Stille, 2001; other anomalies from Lawrence et al., 2006):

$$(La/La^*)_{SN} = La_{SN}/(Pr_{SN} \times (Pr_{SN}/Nd_{SN})^2) \quad (1)$$

$$(Ce/Ce^*)_{SN} = Ce_{SN}/(Pr_{SN} \times (Pr_{SN}/Nd_{SN})) \quad (2)$$

$$(Eu/Eu^*)_{SN} = Eu_{SN}/(Sm_{SN}^2 \times Tb_{SN})^{1/3} \quad (3)$$

$$(Gd/Gd^*)_{SN} = Gd_{SN}/(Tb_{SN}^2 \times Sm_{SN})^{1/3} \quad (4)$$

$$(Y/Y^*)_{SN} = 2 \times Y_{SN}/(Dy_{SN} + Ho_{SN}) \quad (5)$$

The distribution coefficient (D) is a function of the relative uptake of dissolved REEs from water into the precipitated mineral. For seawater, it is empirically expressed as:

$$D^{REE}_{proxy/seawater} = [(REE)_{proxy}/(REE)_{seawater}] \times [Ca_{seawater}/Ca_{proxy}] \quad (6)$$

and the values of $Ca_{seawater}$ and Ca_{proxy} are defined as 0.01 mol/kg and 10 mol/kg, respectively, in the manner of Webb and Kamber (2000).

Comparisons of REE + Y distributions by study site or analytical protocol were made by ratioing individual PAAS-normalized elemental values. For example, $(REE + Y)_{PFA}/(REE + Y)_{PFB}$ represents the ratio of REE + Y distributions for PFA to PFB, a comparison that serves to reveal the effects of siliciclastic contaminants in the bulk sample (PFA) relative to the carbonate fraction (PFB) of the sample. Similar comparisons include $(REE + Y)_{PFB}/(REE + Y)_{PFD}$ (for PFB to PFD), $(REE + Y)_{ooid}/(REE + Y)_{seawater}$ (for ooids to seawater), and $(REE + Y)_{GBB}/(REE + Y)_{GSL}$ (for GBB ooids to GSL ooids).

In addition, the mineral compositions of sampled GSL ooid sands were analyzed using a PANalytical X'Pert Pro MPD X-ray diffractometer (XRD) with Ni-filtered Cu Kα radiation (40 kV and 40 mA) at the China University of Geosciences-Wuhan. Mineral identifications were made by comparison of diffraction patterns with the reference database of the Joint Committee Powder Diffraction Standards. Petrographic observations were performed using a Leica DM2700P polarizing microscope at the Southwest Petroleum University in Chengdu, China. Detailed analyses included examination of ooid morphologies and cortical structures, fossil identification, ooid-size distributions, and point-counting measurements of nuclei to total ooid area on photomicrographs of thin sections with a grid range of 50 μm × 50 μm. The criteria of point-counting were adopted from Flügel (2004).

4. Results

Digestion protocol results of the bulk samples (PFA) and the carbonate and non-carbonate fractions (PFB and PFC) for both GBB and GSL ooids are shown in Table 1 and Fig. 2A–C. The mean elemental values (± 1σ) of all LA spots in ooid cortices at Joulter Cays and Schooner Cays (n = 654) and Antelope Island (n = 333) are also given in Table 1. Individual ooid cortex elemental compositions are summarized in Table S3 and their REE + Y distributions are shown in Fig. 2D–F. Fig. 3 shows ooid morphology and LA spot positions from representative ooid cortices. X-ray diffraction analysis confirms the mineralogic composition of GSL ooid sands at Antelope Island as 67% aragonite, 1% calcite, 17% quartz, 9% orthoclase, and 6% illite (volume estimates). Original elemental data (including fossil, and ooid cortex, fabric, and nuclei information) from each LA spot in GBB (n = 672) and GSL (n = 337) ooids, and the X-ray diffraction pattern of GSL ooid

Table 1
REE characteristics of ooid samples from the Great Bahama Bank and the Great Salt Lake. PFA = Processing flow A (ooid sands dissolved in HNO_3 + HF); PFB = Processing flow B (ooid sands dissolved in CH_3COOH); PFC = Processing flow C (CH_3COOH-insoluble components dissolved in HNO_3 + HF); and PFD = Processing flow D (LA-ICP-MS analysis). Note PFA to PFC analyzed by Agilent 7700x ICP-MS, and PFA* and PFB* analyzed by Thermo Fisher iCAP RQ ICP-MS. The spot numbers acquired from PFD on ooid cortices at Joulter Cays, Schooner Cays, and Antelope Island are 146, 508, and 333 respectively, and their mean values are listed here.

Element (ppm)	PAAS[a]	Surface seawater[b] Value × 10^5	Great Bahama Bank							Great Salt Lake					
			Joulter Cays	Joulter Cays	Schooner Cays	Schooner Cays	Schooner Cays	Joulter Cays	Schooner Cays	Antelope Island					
			PFA	PFB	PFA	PFB	PFB*	PFD	PFD	PFA	PFA*	PFB	PFB*	PFC	PFD
Al								13 ± 21	4 ± 3	2900	2800	181	182	18,900	185 ± 217
Sc			0.174	0.181	0.206	0.085		0.135 ± 0.068	0.120 ± 0.066	6.87	7.00	0.093		16.8	0.177 ± 0.091
Ti								1.030 ± 0.988	0.666 ± 0.379						7.934 ± 8.681
Mn								0.677 ± 0.395	0.762 ± 0.375						5.960 ± 6.298
Fe								149 ± 73	99 ± 38						290 ± 226
Sr								9441 ± 222	9636 ± 289						3977 ± 272
Zr			0.502	0.040	0.575	0.054		0.093 ± 0.044	0.086 ± 0.103	26.2	14.5	0.153		10.2	0.600 ± 0.703
Y	27	1.147	0.79	0.584	1.607	2.099	1.821	0.666 ± 0.203	1.347 ± 0.293	2.97	2.87	3.019	2.394	5.61	1.568 ± 0.299
La	38.2	0.205	0.095	0.044	0.205	0.17	0.184	0.037 ± 0.033	0.110 ± 0.057	1.83	1.69	0.696	0.697	9.46	0.436 ± 0.174
Ce	79.6	0.168	0.167	0.066	0.3	0.215	0.231	0.051 ± 0.053	0.128 ± 0.063	4.14	4.5	1.757	1.746	19.5	1.075 ± 0.445
Pr	8.83	0.044	0.024	0.011	0.046	0.041	0.045	0.010 ± 0.007	0.029 ± 0.016	0.438	0.487	0.178	0.172	2.12	0.109 ± 0.041
Nd	33.9	0.204	0.094	0.055	0.214	0.208	0.21	0.051 ± 0.030	0.143 ± 0.078	1.7	1.58	0.788	0.745	7.7	0.480 ± 0.172
Sm	5.55	0.048	0.016	0.015	0.068	0.056	0.054	0.027 ± 0.011	0.049 ± 0.019	0.401	0.405	0.208	0.186	1.45	0.117 ± 0.042
Eu	1.08	0.014	0.007	0.005	0.018	0.017	0.016	0.008 ± 0.005	0.015 ± 0.006	0.162	0.167	0.05	0.046	0.705	0.031 ± 0.009
Gd	4.66	0.076	0.023	0.023	0.098	0.087	0.093	0.038 ± 0.022	0.082 ± 0.033	0.389	0.393	0.248	0.24	1.4	0.166 ± 0.051
Tb	0.774	0.013	0.008	0.004	0.017	0.015	0.016	0.006 ± 0.003	0.014 ± 0.005	0.062	0.063	0.041	0.039	0.191	0.029 ± 0.008
Dy	4.68	0.096	0.047	0.034	0.122	0.116	0.115	0.037 ± 0.015	0.100 ± 0.031	0.384	0.377	0.288	0.26	1.02	0.206 ± 0.049
Ho	0.991	0.025	0.010	0.010	0.032	0.03	0.029	0.012 ± 0.004	0.027 ± 0.007	0.082	0.08	0.061	0.057	0.21	0.045 ± 0.011
Er	2.85	0.08	0.039	0.035	0.09	0.091	0.085	0.040 ± 0.016	0.083 ± 0.022	0.245	0.241	0.187	0.168	0.653	0.144 ± 0.028
Tm	0.405	0.012	0.005	0.005	0.012	0.012	0.011	0.007 ± 0.002	0.011 ± 0.003	0.035	0.033	0.026	0.024	0.096	0.021 ± 0.006
Yb	2.82	0.072	0.033	0.027	0.069	0.069	0.064	0.040 ± 0.012	0.063 ± 0.017	0.382	0.357	0.16	0.144	0.845	0.137 ± 0.023
Lu	0.433	0.012	0.007	0.006	0.009	0.011	0.01	0.006 ± 0.001	0.010 ± 0.003	0.04	0.037	0.027	0.022	0.118	0.021 ± 0.005
Th			0.031	0.007	0.033	0.015		0.008 ± 0.007	0.011 ± 0.009	3.85	3.52	0.334		23.1	0.355 ± 0.107
ΣREE	184.77	1.07	0.57	0.34	1.30	1.14	1.16	0.37 ± 0.17	0.86 ± 0.32	10.29	10.41	4.71	4.54	45.47	3.02 ± 1.01
Y/Ho	27	47	81	58	51	70	63	60 ± 14	52 ± 9	36	36	49	42	27	35 ± 5
$(Ce/Ce^*)_{SN}$		0.51	0.78	0.81	0.87	0.75	0.70	0.89 ± 0.73	0.72 ± 0.30	1.06	0.87	1.27	1.27	0.97	1.28 ± 0.40
$(La/La^*)_{SN}$		1.57	0.95	1.43	1.49	1.62	1.41	1.34 ± 0.91[c]	1.88 ± 1.24	0.99	0.57	1.21	1.18	0.92	1.27 ± 0.23
$(Gd/Gd^*)_{SN}$		1.24	0.75	1.25	1.18	1.20	1.26	1.45 ± 0.74	1.29 ± 0.34	1.08	1.07	1.13	1.18	1.19	1.18 ± 0.21
$(Eu/Eu^*)_{SN}$		1.17	1.43	1.39	1.11	1.22	1.17	1.49 ± 0.73	1.34 ± 0.51	2.01	2.04	1.10	1.10	2.55	1.16 ± 0.27
$(Y/Y^*)_{SN}$		1.86	2.95	2.50	2.05	2.83	2.52	2.57 ± 0.47	2.12 ± 0.27	1.33	1.32	1.81	1.57	0.97	1.31 ± 0.13
$(Pr/Yb)_{SN}$		0.20	0.23	0.13	0.21	0.19	0.22	0.08 ± 0.05	0.15 ± 0.07	0.55[d]	0.66[e]	0.35	0.38	0.80	0.25 ± 0.07
$(Pr/Tb)_{SN}$		0.30	0.26	0.27	0.24	0.24	0.25	0.17 ± 0.08	0.18 ± 0.06	0.62	0.68	0.38	0.39	0.97	0.34 ± 0.07
$(Tb/Yb)_{SN}$		0.66	0.88	0.49	0.90	0.79	0.91	0.52 ± 0.26	0.82 ± 0.25	0.90[f]	0.98[g]	0.93	0.99	0.82	0.76 ± 0.15

[a] Reference value of Post-Archean Australian Shales (PAAS) from McLennan (1989).

[b] Reference surface REE + Y compositions of seawaters from open oceanic Western Atlantic GEOTRACES inter calibration sample at BATS (close to Bahamas) acquired from 15 m water-depth through 0.2 μm spot-size filter (REE from van de Flierdt et al., 2012; Y from Osborne et al., 2015).

[c] Excludes some extremely high values of ooid cortex (> 3σ; 20%, n = 30) as the result of detection limit effect (see Section 5.1). The original value is 3.15 ± 4.26.

[d–g] The Yb_{SN} is from the mean value of neighboring Tm_{SN} and Lu_{SN} due to a significant positive Yb anomaly occurring in its shale-normalized pattern. For details see Section 3.3. Their original values from d to g are 0.37, 0.44, 0.59, and 0.64, respectively.

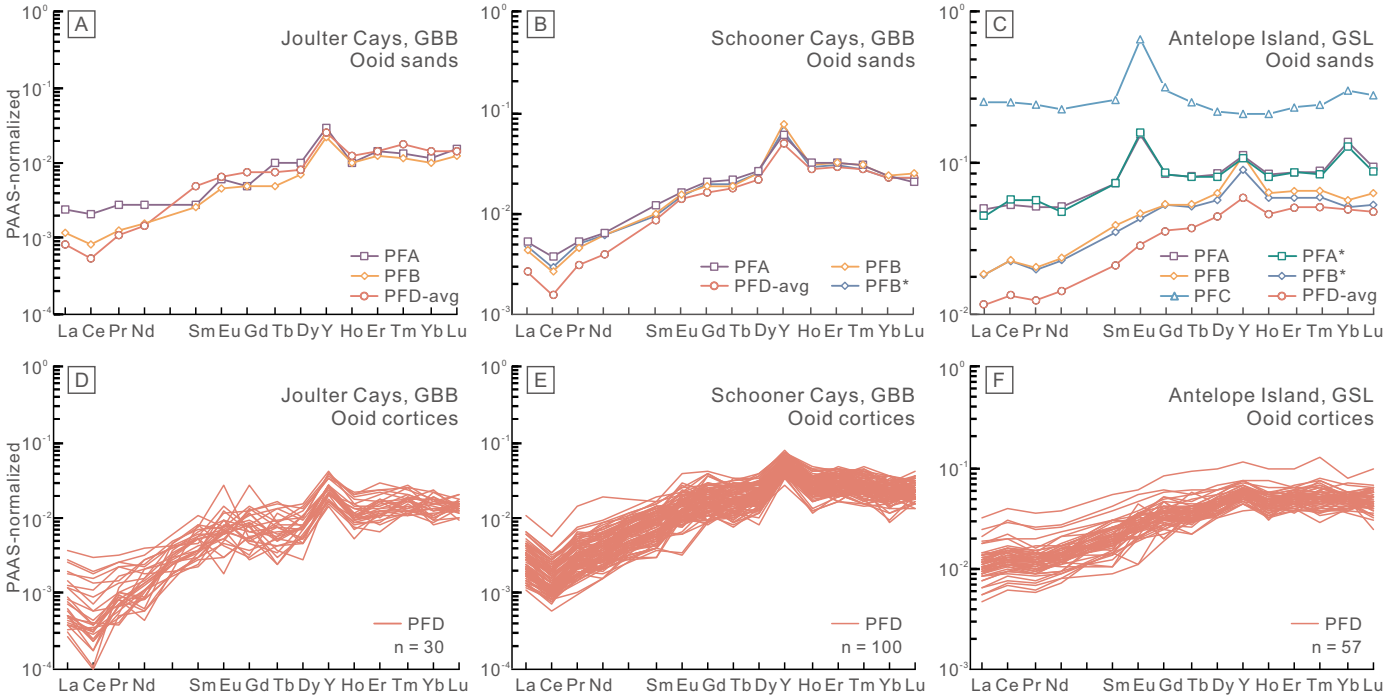

Fig. 2. PAAS-normalized REE + Y patterns of different ooid components from Great Bahama Bank (GBB) and Great Salt Lake (GSL). PFA-PFD are different processing flows shown in Section 3. Datasets marked by an asterisk (e.g. PFA*, PFB*) were analyzed on a Thermo Fisher iCAP RQ ICP-MS, other solution based protocols without an asterisk (PFA to PFC) were analyzed on an Agilent 7700x ICP-MS. (A) Ooid sands (PFA), ooid acetic acid-soluble component (PFB), and ooid cortex (mean value of PFD) REE patterns from Joulter Cays, GBB. (B) Ooid sands (PFA), ooid acetic acid-soluble component, and ooid cortex (mean value of PFD) REE patterns from Schooner Cays, GBB. Note that the acetic acid-insoluble component (PFC) was below detection in this study. (C) Ooid sands (PFA and PFA*), ooid acetic acid-soluble component (PFB and PFB*), ooid acetic acid-insoluble component (PFC) and ooid cortex (mean value of PFD) REE patterns from Antelope Island, GSL. (D)–(E) Mean REE + Y values of laser ablation spots in cortex for individual ooids respectively from Joulter Cays and Schooner Cays. (F) Mean REE + Y values of laser ablation spots in cortex for individual ooids from Antelope Island. All REE values are normalized to Post-Archean Australian Shale (PAAS) (McLennan, 1989).

sands, are given in Tables S4 and Fig. S3, respectively. The characteristics of REE and some trace element compositions at GBB and GSL ooids are summarized in Sections 4.1 and 4.2.

4.1. Bahamian ooid REE compositions

Ooids analyzed by PFA and PFB have similar REE + Y distributions at Joulter Cays and Schooner Cays, but PFA results yield higher REE concentrations (0.57 ppm at Joulter Cays, 1.30 ppm at Schooner Cays) than PFB results (0.34 ppm at Joulter Cays, 1.14 and 1.16 ppm at Schooner Cays; note: two independent results for the latter site) (Table 1; Fig. 2A and B). For the carbonate fractions (obtained by PFB) at the two sites, the REE + Y distributions have similar characteristics, including (1) positive La, Eu, Gd, and Y anomalies, (2) a negative Ce anomaly, (3) high Y/Ho ratios, and (4) depleted LREEs (for summary of original data, see Table 1).

GBB ooid cortices analyzed by PFD (Fig. 2A and B) yielded similar REE + Y distributions relative to PFB results for the same samples, including (1) positive La, Eu, Gd, and Y anomalies, (2) negative Ce anomaly, and (3) higher Y/Ho, but depleted more LREEs ($(Pr/Yb)_{SN}$ = 0.08 ± 0.05 (PFD) vs 0.13 (PFB) at Joulter Cays; $(Pr/Yb)_{SN}$ = 0.15 ± 0.07 (PFD) vs 0.18/0.22 (PFB; n = 2) at Schooner Cays (for summary of original data, see Table 1). The REE + Y signatures generated by PFD at Joulter Cays and Schooner Cays are similar to one another, but some spikes (e.g., Pr, Eu, Ho) and inconsistent signals (e.g., Ce) were noted in their PAAS-normalized patterns, especially for Joulter Cays samples (Fig. 2D and E). Additionally, the Joulter Cays samples yielded a larger proportion of REE results below detection limits (233 out of 2058) than the Schooner Cays samples (234 out of 7395) (for original spot data, see Table S4); the rejected results are discussed in Section 5.1.

4.2. Great Salt Lake ooid REE compositions

PFA results exhibit (1) a positive Y anomaly ($(Y/Y^*)_{SN}$ = 1.33/1.32, n = 2), (2) a depleted LREE pattern ($(Pr/Yb)_{SN}$ = 0.55/0.66), (3) relatively flat MREE and HREE patterns ($(Tb/Yb)_{SN}$ = 0.90/0.98), and (4) a large positive Eu anomaly ($Eu/Eu^*)_{SN}$ = 2.01/2.04) (for summary of original data, see Table 1; Fig. 2C). When comparing with PFA, PFB yields greater LREE depletion ($(Pr/Yb)_{SN}$ = 0.35/0.38) and positive La ($(La/La^*)_{SN}$ = 1.21/1.18), Ce ($(Ce/Ce^*)_{SN}$ = 1.27/1.27), and Y anomalies ($(Y/Y^*)_{SN}$ = 1.81/1.57), and a smaller positive Eu anomaly ($(Eu/Eu^*)_{SN}$ = 1.10/1.10) (Table 1). PFC yields a relatively flat REE + Y distribution ($(Pr/Yb)_{SN}$ = 0.80, $(Pr/Tb)_{SN}$ = 0.97, and $(Tb/Yb)_{SN}$ = 0.82) with a sharp positive Eu anomaly ($(Eu/Eu^*)_{SN}$ = 2.55) (Fig. 2C).

The GSL ooid cortices analyzed by PFD generally show depleted LREEs, positive La, Ce, and Y anomalies, and slightly positive Gd and Eu anomalies (for summary of original data, see Table 1). Relative to GBB ooids, GSL ooids exhibit lower Y/Ho ratios (35 ± 5 vs 52 ± 9 for Joulter Cays and 60 ± 14 for Schooner Cays), higher ΣREE concentrations (3.02 ± 1.01 ppm vs 0.37 ± 0.17 ppm for Joulter Cays and 0.86 ± 0.32 ppm for Schooner Cays), and substantially lower standard errors with respect to mean REE values (Table 1).

5. Discussion

5.1. Detection limit effect

A subset of LA analytical spots (467 out of 9453) yielded REE concentrations that were close to or below the detection limit for the LA-ICP-MS working conditions of this study (Table S4). Elemental concentrations below the instrumental detection limit were more

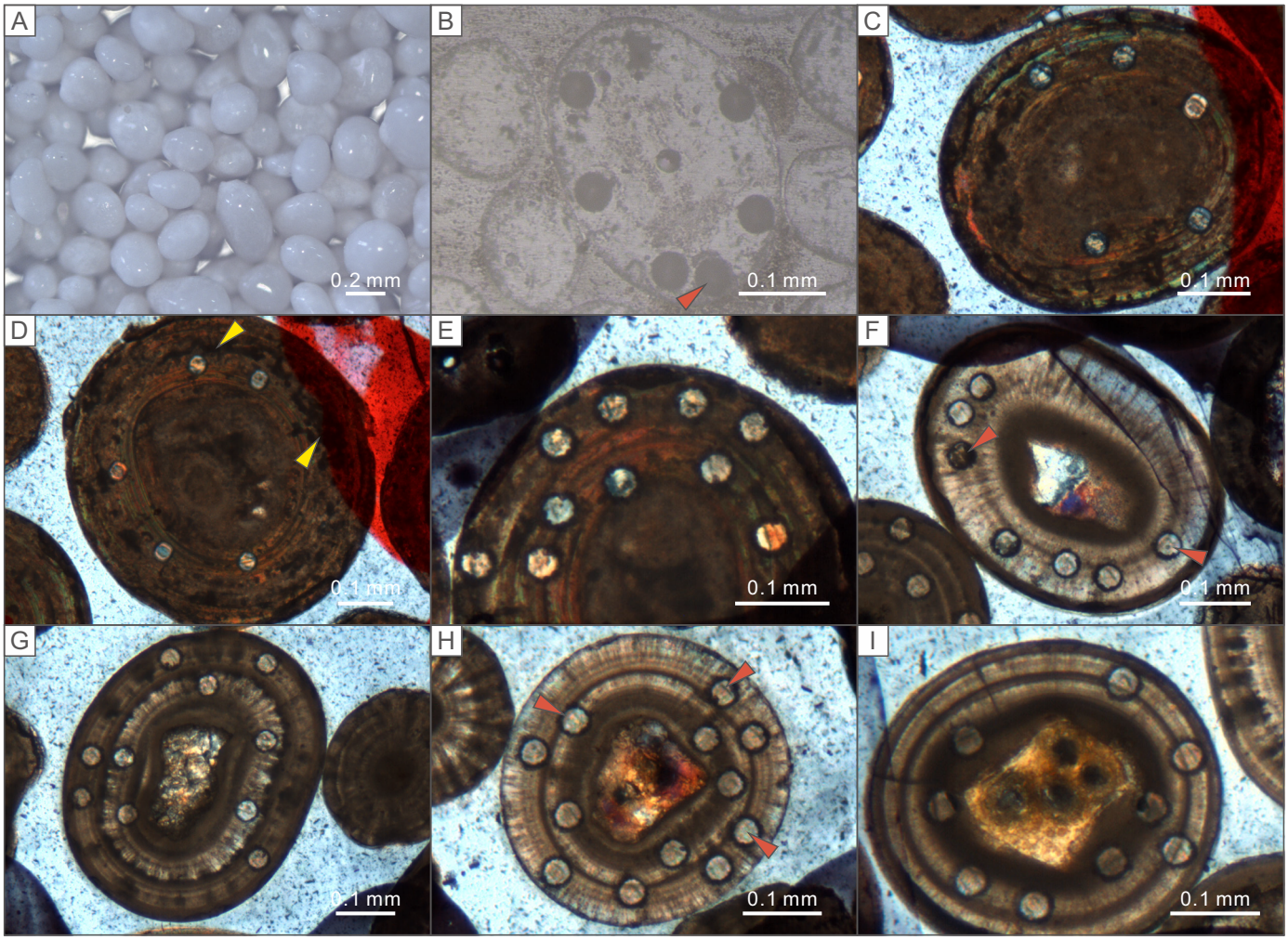

Fig. 3. Photomicrographs of ooids. (A) Schooner Cays ooids with polished, clean surfaces free of apparent siliciclastic particles. (B) Reflected light image of sectioned Joulter Cays ooid (No. Q-2-66 to -70) with laser ablation spots in cortex beyond nucleus. Red arrow marks a canceled spot touching neighboring epoxy in intergranular space. (C) Schooner Cays ooid grain (No. Ba-6-31 to -35) showing five laser-ablation spots on its inner cortex. (D) Endolithic microborings (yellow arrows) in Schooner Cays ooid grain (No. Ba-6-26 to -30). (E) Laser ablation spots in outer (No. Ba-6-101 to -105) and inner (No. Ba-6-106 to -110) ooid cortex at Schooner Cays. (F) Translucent, fine radial ooid with laser ablation spots (No. GS-5-31 to -35) from Antelope Island. It is the least-contaminated ooid cortex (mean Zr = 0.096 ppm) in this study in the GSL. Note red arrows indicate two contaminated spots evidenced by slightly increased Zr and Al (not used in this study). (G) Antelope Island ooid with fine, radial-concentric outer cortex (No. GS-5-36 to -40) and translucent, radial inner cortex (No. GS-5-41 to -45) separated by a possible dissolution surface characterized by irregular terminations of aragonite crystals. (H) Antelope Island ooid with translucent, radial-concentric, outer cortex (GS-5-46 to -50), and darker inner micritic cortex (GS-5-51 to -54). Red arrows indicate contaminated spots which were excluded from the study. (I) Antelope Island ooid with similar fabric to (H), but with a less-contaminated micritic inner cortex (No. GS-5-81 to -84). The original REE data of laser ablation spots shown in Table S4. Note (A) and (B) under reflected light; (C) to (I) under transmitted light. (For interpretation of the references to color in this figure legend, the reader is referred to the web version of this article.)

common in samples with low ΣREE concentrations. The low-ΣREE samples yield more variable $(Ce/Ce^*)_{SN}$ ratios (ca. 0–3) than samples with higher ΣREE, for which $(Ce/Ce^*)_{SN}$ values determined by PFD gradually approach those obtained by PFB with increasing ΣREE (Table 1 and Fig. 4A). The $(Ce/Ce^*)_{SN}$ values of the low-ΣREE ooids are also more variable than those of filtered surface seawater (0–50 m) samples from the Western Atlantic (van de Flierdt et al., 2012; Osborne et al., 2015; Schlitzer et al., 2018), which exhibit $(Ce/Ce^*)_{SN}$ = 0.35–0.75 (Fig. 4A; seawater data summarized in Table S5). Similar patterns are observed for Y/Ho ratios as well as Eu, Gd, and Y anomalies (Fig. S4), suggesting that the increased variability is a product of low ΣREE.

On the other hand, for ooid cortices having higher ΣREE concentrations, the detection limit effect disappears, and the greater uniformity of measured values lends confidence to calculation of anomalies. To test the influence of the detection limit effect on our dataset, ooid cortical data were grouped into bins by ΣREE concentrations (in intervals of 0.1 ppm ranging from < 0.5 ppm to > 1.3 ppm, designated as groups *a* to *j*). The results (Fig. 4B) show increasingly uniform values for $(Pr/Yb)_{SN}$ (from Group *a* (0.07) to *j* (0.24)) that trend towards the western Atlantic surface seawater composition (0.21 ± 0.02) (Table S5). Thus, ooids with the highest ΣREE concentrations (> 1.3 ppm) show the smallest detection limit effect. Comparison of results for other groups to Group *a* allows determination of which groups have been influenced by the detection limit effect. Groups *b* to *e* (i.e., ΣREE = 0.9–1.3 ppm) yield REE distributions similar to Group *a*, but groups *f* to *j* (i.e., ΣREE < 0.9 ppm) exhibit large relative errors and significantly decreased cohesion in LREE and MREE depletions (of > 50% on the logarithmic ordinate; Fig. 4C). Hence, PFD analyses of samples with ΣREE content > 0.9 ppm (n = 41; note all Joulter Cays ooid cortices were excluded) do not show a detection limit effect and can be regarded as reliable proxies for seawater chemistry.

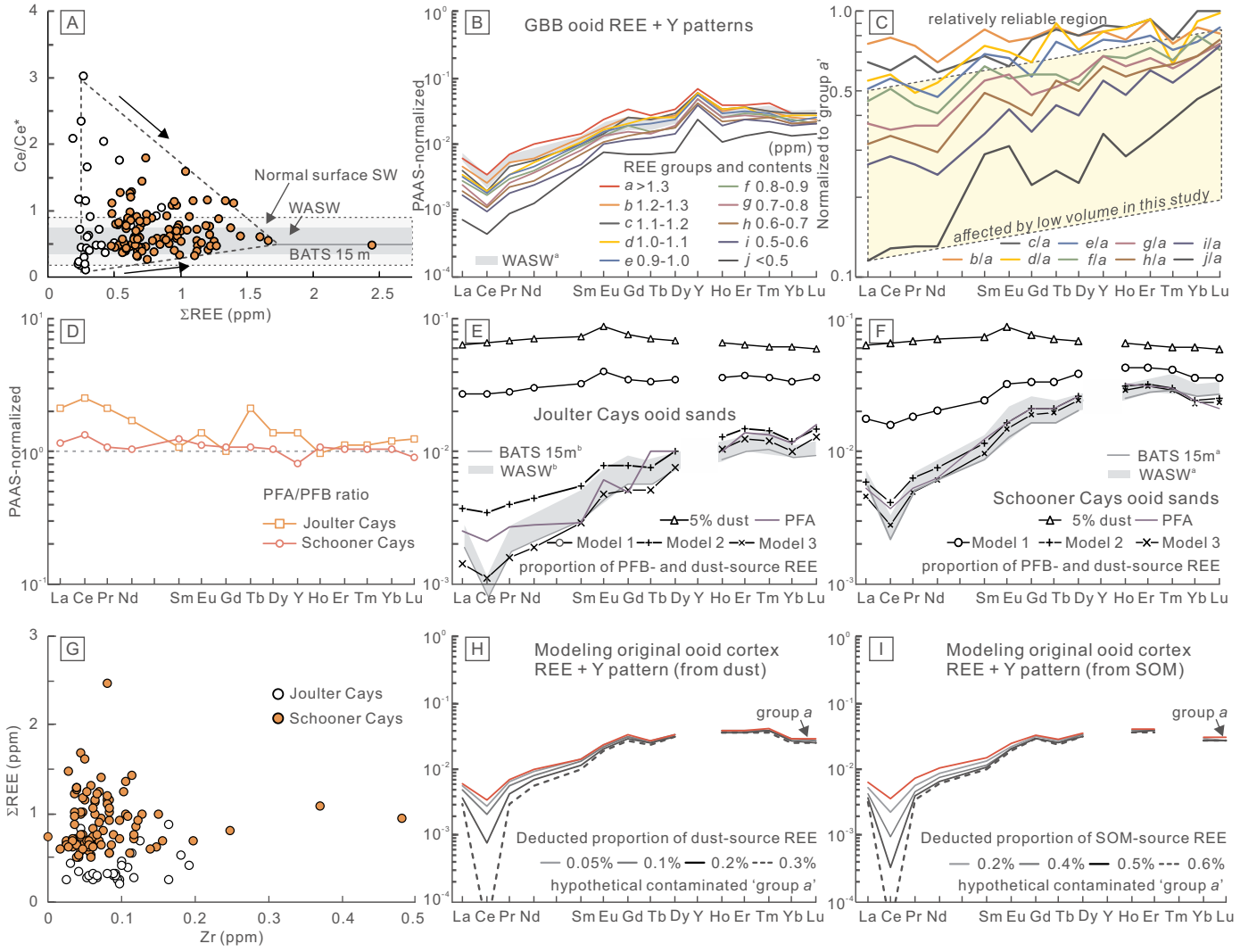

Fig. 4. (A) ΣREE concentrations versus Ce anomaly. The Ce/Ce* shows a wide range of values at low REE concentrations but gradually converge on normal surface seawater (SW), Western Atlantic surface waters (WASW; < 50 m), and open-marine surface seawater (15 m depth) at Bermuda Atlantic Time-Series Study station (BATS 15 m) levels with increasing concentration (original seawater data summarized in Table S5). (B) PAAS-normalized REE + Y patterns of analyses grouped by REE concentrations (*a* to *j*) in 0.1 ppm increments, and the comparison with WASW[a] pattern ($\times 10^5$). (C) Mean REE value from groups *b* to *j* (in B) normalized to 'group *a*', respectively. Note the increasing cohesion with greater concentration suggesting effects of low element concentrations combined with small sample volume in LA technique; large relative errors at low concentrations do not allow robust anomaly calculation. For details see Section 5.1 (D) Total digestion (PFA) of GBB ooid sands normalized to the acetic acid-soluble component (PFB), suggesting that insoluble component at Joulter Cays is enriched in LREEs and some MREEs. No marked difference between PFA and PFB exist at Schooner Cays (except for Ce and Y). (E) and (F) Hypothetical mixing of siliciclastic REE source (i.e. African dust) with Bahamian ooid carbonate components (represented by PFB) to model degrees of contamination. Models 1 to 3 in (E) indicate 98% PFB + 2% dust, 99.8% PFB + 0.2% dust, and 99.98% PFB + 0.02% dust components, respectively. Models 1 to 3 in (F) indicate 99% PFB + 1% dust, 99.9% PFB + 0.1% dust, and 99.99% PFB + 0.01% dust components, respectively. This shows that no more than 0.2% and 0.1% REE compositions (by volume) originated from dust in the Joulter Cays and Schooner Cays ooid sands, respectively. The REE distributions of WASW (< 50 m) and BATS 15 m are shown for reference (original seawater data summarized in Table S5). The values of BATS 15 m[b] and WASW[b] in (E) are seawater REE concentrations × 0.3 × 10^5; the values of BATS 15 m[a] and WASW[a] in (F) are seawater REE concentrations × 10^5. (G) Zr content versus ΣREE concentrations. (H)–(I) Two model calculations show possible original REE patterns from admixture of increasing proportions of dust- and organic matter-sourced REEs within ooid cortex. Note the 'group *a*' (red line) is inferred to have been contaminated by dust- and organic matter-sourced REEs; the proportion of mixed contamination within ooid cortices is extremely low, and has little influence on its REE pattern except for Ce. For details see the texts in Section 5.2.1. African dust REE data from Pourmand et al. (2014); Sedimentary organic matter REE data from Freslon et al. (2014). (For interpretation of the references to color in this figure legend, the reader is referred to the web version of this article.)

5.2. REE + Y signatures in Great Bahama Bank ooids

5.2.1. Siliciclastic impurities

Because of limited recovery of non-carbonate material during PFC analysis of GBB ooids, the most efficacious method of determining the composition of their siliciclastic fraction proved to be comparison of their whole-rock (PFA) and carbonate-fraction (PFB) REE + Y signatures. GBB ooids are nearly pure carbonate (> 99%) in composition, and PFA and PFB yielded similar REE + Y distributions (Table 1). However, the PFA results reflect the presence of a minor, but measurable, siliciclastic fraction. In the Joulter Cays samples, some siliciclastically sourced elements show much higher concentrations in the bulk sample (PFA) (Zr = 0.50 ppm, Th = 0.031 ppm) than in the carbonate fraction (PFB) (Zr = 0.040 ppm; Th = 0.007 ppm). A similar pattern is observed in the Schooner Cays sample (Table 1). The ratio of PFA to PFB for REE + Y distributions (i.e., $(REE + Y)_{PFA}/(REE + Y)_{PFB}$) yields a nearly flat pattern with slightly positive Ce and negative Y anomalies in the Schooner Cays samples, but greater enrichment of LREEs and

some MREEs (Eu, Tb and Dy) in the Joulter Cays samples (Fig. 4C). At Joulter Cays, the carbonate fraction shows a relative depletion of LREEs ($(Pr/Yb)_{SN}$ = 0.13) compared to the bulk sample ($(Pr/Yb)_{SN}$ = 0.23), but at Schooner Cays there is little difference between the carbonate fraction and bulk sample values (Table 1). Thus, the non-carbonate fraction is responsible for a pronounced modification of the original carbonate REE + Y signal in the Joulter Cays bulk ooid sands, especially with regard to the LREEs.

Modeling calculations suggest that even a very minor admixture of dust would have been sufficient to modify the bulk REE + Y compositions of Bahamian ooid sands. African dust is the main source of non-carbonate material in the Bahamas, and it has a mean ΣREE of 246.9 ppm (Pourmand et al., 2014). Fig. 4E and F show that only ~0.02–0.2% and ~0.01–0.1% of admixed African dust (by volume) are necessary to alter the LREE distribution of pure carbonate sediment owing to the extremely low REE content of the latter. For example, at Joulter Cays, an admixture of 0.1% dust contributes ~0.25 ppm to ΣREE, which is similar to the ΣREE (0.34 ppm) of the much larger volume of carbonate host rock (99.9%). The lesser amount of dust present at Schooner Cays relative to Joulter Cays may be related to the stronger currents at the former locale (Bergman et al., 2010), as supported by the quantitative statistics of ooid sizes (see Section 2.1). In such high-energy settings, fine sediment (e.g., dust) may be preferentially winnowed out of the surface sediments more easily.

Admixture of dust and detrital organic matter may also influence marine carbonate REE + Y compositions, and the degree of their influence on seawater-precipitated ooid cortices needs to be evaluated. Modeling calculations show that contamination from these sources has only a weak influence on GBB ooid cortex REE + Y patterns when the proportions of these admixed components are < 0.2% and < 0.5% (by volume), respectively (black solid lines in Fig. 4H and I). Larger amounts of exogenous contamination within GBB ooid cortices (e.g., > 0.3% dust-sourced or > 0.6% organic matter-sourced REEs; dashed lines) are unlikely because the Ce values in these admixed components would be even higher than in ooid cortex (i.e., 'group *a*') (Fig. 4H and I). Zr, which is a useful proxy for siliciclastic contamination, shows generally low concentrations (Fig. 4G), especially in samples with higher ΣREE concentrations (> 1.3 ppm) in which mean Zr content is 0.073 ± 0.032 ppm (Fig. 4B). Furthermore, Zr exhibits no significant correlation to ΣREE content (Fig. 4G), so evidence for contamination from siliciclastic particles or sedimentary organic matter in the GBB ooid cortices (note: not ooid sands) is not obvious.

5.2.2. Carbonate fraction (seawater signal)

In contrast to the sample digestion protocols (PFA to PFC), in situ LA-ICP-MS analysis (PFD) can reveal fine-scale compositional variation within individual ooids. For both Joulter Cays and Schooner Cays samples, the PFB and PFD methods yielded similar patterns, especially with regard to MREEs and HREEs (Fig. 2A and B; Table 1). Within single Bahamian ooids, the outer and inner parts of the cortex commonly have nearly uniform ΣREE concentrations and REE + Y characteristics except for some ooids showing slight contamination in PFD results (e.g., Fig. 3E, see Fig. S4-A for its REE + Y pattern). Given a LA analytical spot size of 44 μm and the limited thickness of GBB ooid cortices (~0.05–0.5 mm; e.g., Fig. 3B), it seems likely that some inner-cortex measurements have partly sampled ooid nuclei (e.g., Fig. S4-E). Nuclei consisting of foraminifer tests (e.g., Fig. S4-B and -G) have little effect on measured REE + Y patterns because their REE content is also seawater-derived (Byrne and Kim, 1990; Osborne et al., 2017). Other bioclasts (e.g., algae and gastropods) were not analyzed successfully by the PFD method at Sample-Solution Analytical Laboratory in Wuhan due to their extremely low REE content (e.g., Webb and Kamber, 2000), but results from the University of Queensland show LREE-depleted patterns (no negative Ce anomalies) with some spikes (Fig. S4-F). Contamination by nuclei composed of the latter bioclasts would markedly affect interpretations of ooid cortical chemistry (e.g., Zhang et al., 2017).

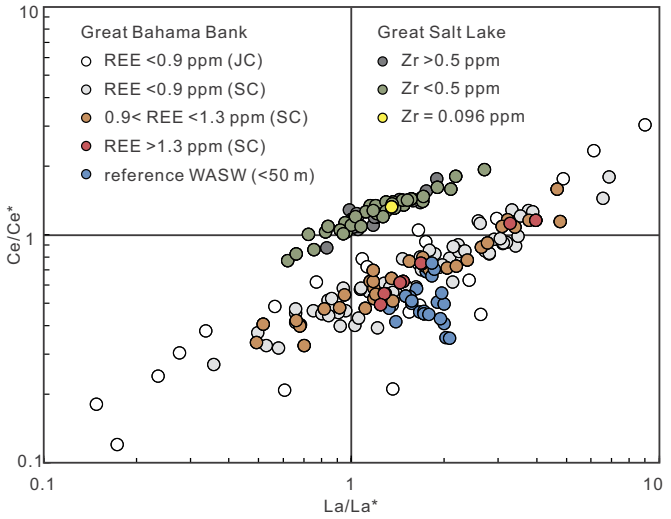

Fig. 5. La versus Ce anomalies for GBB and GSL ooid cortices obtained by laser ablation. JC = Joulter Cays; SC = Schooner Cays. Reference seawater data from WASW (< 50 m, n = 22; original data summarized in Table S5). Anomalies of La and Ce calculated using the method of Lawrence and Kamber (2006).

When used as a paleo-seawater redox proxy, Ce anomalies in carbonates are ~0.4–0.5 for oxic waters and ~0.9–1.0 for anoxic waters (Elderfield and Greaves, 1982; German and Elderfield, 1990) Thus, it is necessary to explain the occurrence of high $(Ce/Ce^*)_{SN}$ within reliable GBB ooid cortices that formed in oxic surface seawater (including some values > 1; Fig. 5). These ooid cortices yield mostly positive La anomalies (80%, n = 41) and negative Ce anomalies (80%, n = 41) as a function of the equations of Lawrence and Kamber (2006), for which a $(Ce/Ce^*)_{SN}$ value of ~0.4 would be expected. Although the mean values of La and Ce anomalies for reliable ooid cortices conform to the results from carbonate fractions of ooids sands (PFB) and neighboring surface seawater (Table 1), 39% of our analyses plot outside of this region (Fig. 5). The spread in $(Ce/Ce^*)_{SN}$ values may be due to microscale heterogeneity in ooid cortical compositions related to the presence of microborings and organic matter (Figs. 3D and S1). One possibility is that the formation of ooid laminae can occur as a result of increased alkalinity driven by microbial respiration of organic matter using SO_4^{2-} or NO_3^- (Reid and Macintyre, 2000; Andres et al., 2006; Diaz et al., 2015). Such microbial metabolisms typically dominate in anoxic pore waters or microenvironments, and they may have contributed to the weak negative to minor positive Ce anomalies observed in some ooid laminae.

The similarity of the REE + Y distribution of GBB ooid cortices to that of Atlantic Ocean surface waters suggests that GBB ooids are a robust recorder of seawater REE + Y chemistry. This comparison is based on filtered surface seawaters from the Western Atlantic GEOTRACES intercalibration sample at BATS 15 m (van de Flierdt et al., 2012) and from the neighboring WASW (Osborne et al., 2015; Schlitzer et al., 2018) (for summary of original data, see Table S5). Normalization to the BATS seawater results in a relatively flat pattern wherein REE distribution coefficients for PFD (D_{PFD} = 116 ± 21) are similar to the values for PFB (D_{PFB} = 108 ± 14 and 108 ± 16; two independent results) of Schooner Cays ooids (Fig. 6A). Thus, the range of ooid distribution coefficients is lower than for reefal microbialites (Webb and Kamber, 2000) but higher than for corals (Sholkovitz and Shen, 1995) and bivalves (Ponnurangam et al., 2016) (Fig. 6B). The range of D_{ooid} values overlaps those of some types of unburied foraminifer tests (Palmer, 1985; Osborne et al., 2017) and brachiopod shells (Zaky et al., 2016a, 2016b) in modern oceans. Despite similar values, the flattened

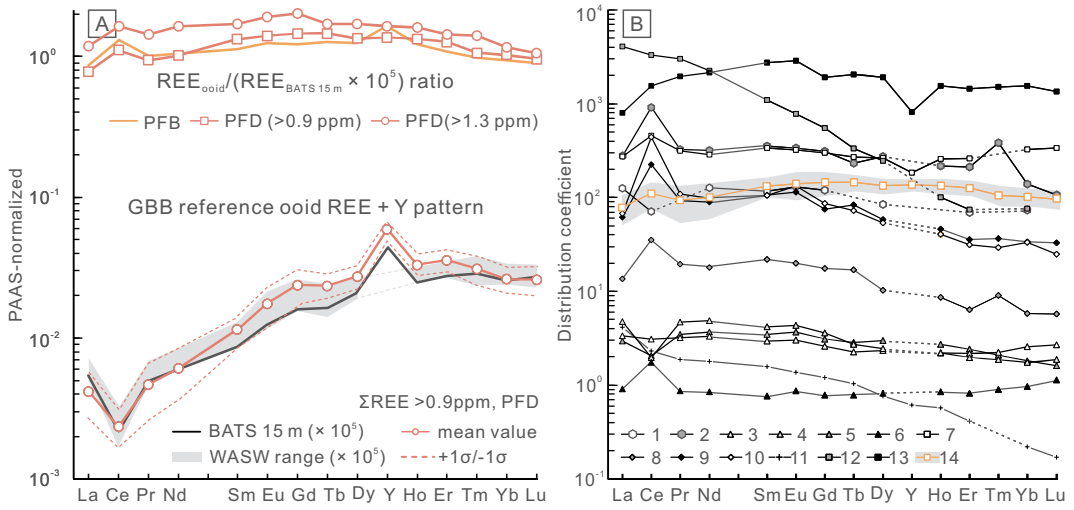

C Reference ooid cortical REE+Y values (Schooner Cays; PFD method, ΣREE >0.9ppm; Unit: ppm)

	La	Ce	Pr	Nd	Sm	Eu	Gd	Tb	Dy	Y	Ho	Er	Tm	Yb	Lu
Mean	0.159	0.185	0.041	0.205	0.063	0.019	0.110	0.018	0.129	1.607	0.033	0.102	0.013	0.074	0.011
σ	0.058	0.059	0.018	0.087	0.015	0.006	0.032	0.004	0.024	0.239	0.006	0.019	0.003	0.016	0.003

Fig. 6. (A) Range of PAAS-normalized ooid cortical REE + Y compositions (mean value ± 1σ; ΣREE > 0.9 ppm) for GBB ooids, and comparisons with neighboring well analyzed surface seawaters at BATS 15 m (van de Flierdt et al., 2012; Osborne et al., 2015), and summarized range of WASW (< 50 m; Table S5). Note relatively flat distribution of mean GBB ooid cortex (with ΣREE > 0.9 ppm and > 1.3 ppm from method PFD, and ΣREE = 1.15 ppm from method PFB, respectively) normalized to BATS 15 m water (×10^5). (B) REE + Y distribution coefficient patterns for ooids and other carbonate precipitates from ambient waters. 1. Planktic foraminifers (Palmer, 1985). 2. Benthic foraminifers (Haley et al., 2005). 3–6. Corals: *Oulastrea crispate*, *Porites lutea* cf., *Goniastrea pectinate*, and *Stylophora pistillata*, respectively (Akagi et al., 2004). 7. Reefal microbialite (Webb and Kamber, 2000). 8–10. Shallow-water terebratulid brachiopod and two deep-water terebratulid brachiopods (Zaky et al., 2016b), respectively. 11. Bivalve *Mytilus edulis* (Ponnurangam et al., 2016). 12. Synthetic calcite grown from seawater solution (Zhong and Mucci, 1995). 13. Calcite precipitated from experimental solution (Tanaka and Kawabe, 2006). 14. GBB ooid reference mean value (ΣREE > 0.9 ppm) and its range (± 1σ) in gray shading (this study). (C) Recommended ooid cortical REE + Y values acquired by PFD with ΣREE > 0.9 ppm at Schooner Cays. Note all ooid data from Joulter Cays are excluded in light of their low ΣREE contents (i.e., < 0.9 ppm).

pattern of D_{ooid} is distinctly different from those of experimentally precipitated and natural skeletal (e.g., foraminifer and brachiopod) calcite minerals, although it resembles those of natural non-skeletal (microbialite) and skeletal (e.g., coral) aragonite minerals (Fig. 6B).

5.3. REE + Y characteristics of Great Salt Lake ooids

5.3.1. Siliciclastic impurities

Unlike the GBB samples, the GSL samples yield different REE + Y patterns for processing flows PFA to PFD, with the results obtained from PFC being especially different. The acetic acid-insoluble fractions (PFC), which consist of quartz, feldspar and illite, have REE + Y characteristics similar to those of fine sediment (silt and clay) in some terrigenous waters (Fig. 7A). The flattened REE + Y pattern with a positive Eu anomaly may indicate fluvial input of sediment derived from a region of volcanic rocks (Fig. 7A), which is consistent with extensive exposures of volcanic rocks to the north and west of the GSL in northern Utah (Jones et al., 2009). In order to investigate the relative contributions of the carbonate and non-carbonate fractions to the GSL bulk-sample REE + Y signatures (PFA), the compositions of the acetic acid-soluble (PFB) and -insoluble (PFC) fractions were used to model mixing patterns. This analysis shows that the REE + Y patterns of bulk samples conform well to a mixture (by volume) of 85% acid-soluble (carbonate) and 15% acid-insoluble REE + Y sources (Fig. 7B).

The results of the PFB and PFD methods show recognizable differences in concentrations of REEs and degree of LREE depletion (Table 1 and Fig. 2C). Differences in ΣREE concentration and $(Pr/Yb)_{SN}$ between PFB and PFD were not caused by admixture of REEs from other types of carbonate components because such non-ooid carbonate components comprise < 1% of GSL samples (by volume). Ratios of PFB and PFD REE + Y distributions (i.e., $(REE + Y)_{PFB}/(REE + Y)_{PFD}$) result in smooth and uniform, slightly LREE-enriched patterns with small Y anomalies (Fig. 7C). It is unlikely that the differences in REE + Y patterns between PFB and PFD are derived mainly from the organic fraction because organic matter is relatively immune to dissolution in mild (1 N) acetic acid (Bayon et al., 2002), and the organic matter-sourced REE + Y distribution shows little relationship to $(REE + Y)_{PFB}/(REE + Y)_{PFD}$ (Fig. 7C and G).

Although silicate minerals (quartz and feldspar) are also difficult to dissolve in 1 N acetic acid, the clay mineral fraction (~6% by volume, consisting mostly of illite) may be primarily responsible for the differences in REE + Y patterns. First, illite can be weakly dissolved in acetic acid (Meredith, 1961; Chester and Hughes, 1967), and any adsorbed REEs and other trace elements (e.g., Al and Zr) may have been released into solution during PFB (Tostevin et al., 2016). This inference is supported by the values of Al and Zr yielded by PFB, which are much higher than for GBB ooids analyzed with the same method (Table 1). Similar results were observed for the least-contaminated GSL ooid cortex based on PFD as well (i.e., Al = 45 ppm, Zr = 0.096 ppm) (Fig. 7E). Second, the LREE-enriched pattern and Y peak of $(REE + Y)_{PFB}/(REE + Y)_{PFD}$ compare well with modern illite-dominated, fine-grained river sediments, e.g., from the Han River (Song and Choi, 2009) and Red River (Bayon et al., 2015) (Fig. 7C). Thus, an illite-based REE source may have affected the results obtained by the PFB method in the GSL ooid digestions.

Given the presence of siliciclastic material within the ooid cortices suggested by the concentrations of Al and Zr, it is necessary to address the distribution and potential influence of siliciclastic materials on GSL ooid cortical REE + Y signatures. Some anomalous signals related to contaminated ooid cortical layers were screened out on the basis of high Al and Zr contents in PFD (marked with red arrows in Fig. 3F and H). This inference is supported by a positive correlation between Zr and

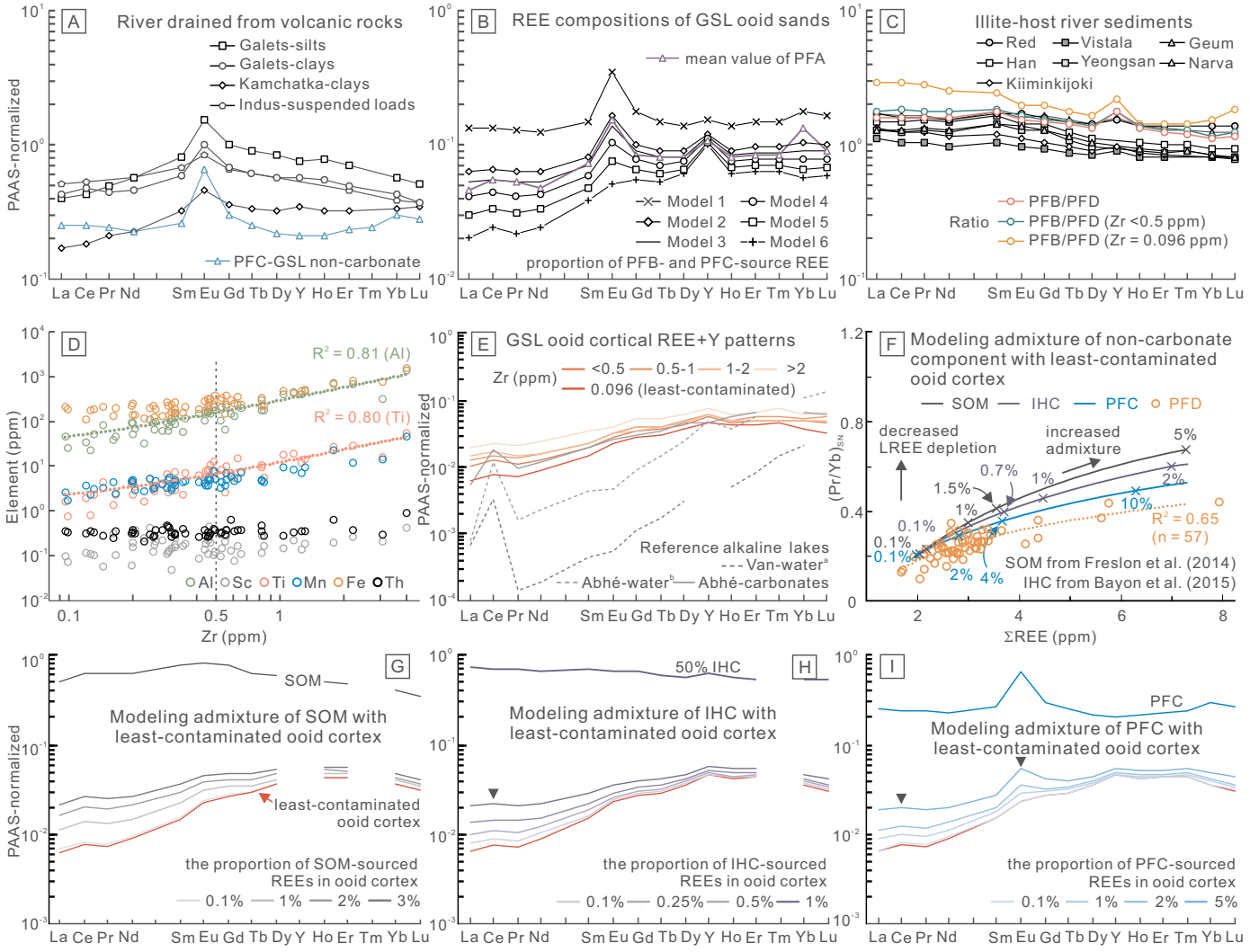

Fig. 7. (A) Comparison of REE patterns in siliciclastic components (represented by PFC) in GSL ooids and river sediments draining volcanic areas. River sediment data from Goldstein and Jacobsen (1988) and Bayon et al. (2015). (B) Hypothetical mixing (by volume) of measured siliciclastic component (represented by PFC) and ooid carbonate component (represented by PFB) to model REE + Y compositions of GSL ooids. Models 1–6 represent 50% PFB + 50% PFC, 80% PFB + 20% PFC, 85% PFB + 15% PFC, 90% PFB + 10% PFC, 95% PFB + 5% PFC, and 99% PFB + 1% PFC components, respectively. (C) Comparison of PAAS-normalized REE patterns of illite-rich river sediments and three different ratios for weak-acid-digestion components (PFB) to ooid cortices (respectively from (1) mean value of PFD, (2) mean value of pure ooid cortices (Zr < 0.5 ppm), and (3) least-contaminated ooid cortex (Zr = 0.096 ppm) in PFD). The slight LREE enrichment of PFB relative to PFD may reflect release of REEs from illite during acetic acid digestion. River sediment data from Song and Choi (2009) and Bayon et al. (2015). (D) Zr versus metals (Al, Sc, Ti, Mn, Fe, and Th) for GSL ooid cortices by PFD. Note that Zr has positive correlations with Al and Ti ($r = +0.90$, $p(\alpha) < 0.01$; $r = +0.90$, $p(\alpha) < 0.01$; $n = 57$), as expected, but positive correlations of Zr with Fe and Mn are more distinct where Zr > 0.5 ppm. There are no significant correlations of Zr with Sc and Th ($r = +0.34$, $p(\alpha) < 0.01$; $r = +0.57$, $p(\alpha) < 0.01$; $n = 57$). (E) PAAS-normalized REE + Y patterns for ooid cortices with different cohorts of Zr values, and the comparison with modern Lake Van and Lake Abhé. Van-water[a] (lake-water REE concentrations × 10^3) data of Lake Van from Möller and Bau (1993); Abhé-water [b] (lake-water REE concentrations × 10^3) and carbonate data of Lake Abhé from Dekov et al. (2014). (F) ΣREE content versus $(Pr/Yb)_{SN}$ ratio for GSL ooid cortices, and from mixing models with sedimentary organic matter (SOM), acetic acid-insoluble components from PFC (PFC), and illite-hosted clay minerals (IHC). The trend line of $(Pr/Yb)_{SN}$ is shown with coefficients of determination (R^2). For reported ΣREE values of SOM, Tm concentrations are based on neighboring Er_{SN} and Yb_{SN} values. (G-I) Hypothetical mixing of three non-carbonate components (SOM, PFC, and IHC) with least-contaminated GSL ooid cortex to illustrate influences on ooid cortical REE distributions. All data from GSL ooids were obtained by LA-ICP-MS in this study. SOM-REE data from Freslon et al. (2014), and IHC-REE data from Bayon et al. (2015).

other metals (e.g., Al, Ti, Mn, Fe) within ooid cortices, but the concentrations of Sc and Th (which are commonly used as proxies for terrigenous contamination) do not show significant correlations with Al and Zr (Fig. 7D). Other indicators of potential siliciclastic contamination include (1) dissolution/defective layer boundaries (e.g., inner cortex of Fig. 3G) in irregularly radial cortices, and (2) elevated and flattened LREE patterns combined with high Zr content (e.g., Fig. S5-A). These features are in contrast to the uniform radial or radial-concentric outer-cortical layers and low Zr contents (< 0.5 ppm) of ooids inferred to have less siliciclastic contamination (Fig. 3F and G; see 7E (red line) and S5-A for their patterns). A promising LA mapping method may be helpful to evaluate the contamination of exogenous-sourced particles by examining the enrichment of LREEs (e.g., Ulrich et al., 2009) or spatial distributions of $(Pr/Yb)_{SN}$.

Modeling can assist in evaluating the degree of REE + Y contamination from non-carbonate components. In our model, REE fractions sourced from sedimentary organic matter (Freslon et al., 2014), illite-hosted clays (Bayon et al., 2015), and acetic acid-insoluble components (obtained by PFC) were mixed on a volume basis with the REE content of the least-contaminated ooid cortex (i.e., Fig. 3F, GS-5-31-35

Table 2
A preliminary evaluation regarding the analyzing qualities and results of REE + Y concentrations with different procedures on carbonate rocks.

Analytical techniques	PFA	PFB	PFC	PFD
	(Strong acid digestion)	(Weak acid digestion)	(non-carbonate digestion)	(In situ laser ablation)
Data source	Carbonate rocks	Carbonate component	Non-carbonate component	From pure to impure carbonates
Data for very pure carbonates	Good	Very good	None	Good
Data for slightly contaminated carbonates	Bad	Very good	None	Good
Data for moderately contaminated carbonate	None	Probably need sequential leaching procedure	None	Need sufficient spot data
Signatures of Ce anomaly and Y/Ho	Stability	Stability	Stability	Variability for heterogeneous components
REE + Y pattern	Stability	Stability	Stability	Depending on spot position
Pretreatment procedure	Easy (generally)	Complicated	Complicated	Easy
Fine-scale analysis	None	Complicated	None	Easy
Overall geochemical data quality	High	High	High	Not good for low values and sparse spots

with the lowest Zr content of 0.096 ppm and a ΣREE of 1.93 ppm). Admixtures of REEs from each of these three contaminant sources resulted in a gradual modification of the REE + Y distributions and Ce and Eu anomalies of the modeled ooid cortices (Fig. 7G–I). Our calculations suggest that the largest effect on Eu anomalies is from the PFC-derived REE fraction, and both illite and PFC-derived REE fractions influence Ce anomalies to a greater degree than organic matter (Fig. 7G–I). In light of the positive correlation between LREE depletion and ΣREE ($r = +0.77$, $p(\alpha) < 0.01$, $n = 57$), our modeling results indicate maximum contaminant REE admixtures to ooid cortices of no more than 0.7%, 1.5%, and 4% sourced from illite-hosted clay, organic matter, and PFC-derived REE fractions, respectively (Fig. 7F). To reconstruct aqueous REE + Y signatures from GSL ooid cortical compositions obtained by PFD, a conservative cutoff of Zr < 0.5 ppm was applied to reduce the effect of silt and clay contamination (Fig. 7D) on REE + Y distributions (Fig. 7E). Thesefore, in situ LA-ICP-MS analysis (PFD) is valuable in facilitating recognition and exclusion of analyses with siliciclastic contamination based on, for example, co-occurring measured Al, Ti, and Zr concentrations on a spot by spot basis (Fig. 7).

5.3.2. Carbonate fraction and positive Ce anomalies in GSL ooids

The GSL ooids generally show uniform HREE-enriched REE + Y distributions and small positive Ce anomalies that are substantially different from those of most shallow-marine sediments but that conform well to some alkaline lacustrine waters and their associated carbonate sediments (Figs. 2F and 7E). A La-vs-Ce anomaly crossplot for GSL ooid cortices ($n = 57$) shows a trend dominated by positive La and Ce anomalies (73%), although smaller numbers of samples yield positive Ce and negative La anomalies (19%) or negative La and Ce anomalies (8%; Fig. 5). There is a strong positive correlation between La and Ce anomalies for samples with Zr < 0.5 ppm ($r = +0.96$, $p(\alpha) < 0.01$, $n = 37$). These observations imply a nearly uniform geochemical behavior of carbonate precipitates under alkaline conditions. Both the acetic acid-soluble fraction and the ooid cortices analyzed using LA yield a pure carbonate REE + Y signature that is characterized by more positive Ce anomalies than the bulk ooid sands or the acetic acid-insoluble particles (Table 1 and Fig. 2C). Thus, the Ce anomalies of GSL ooids appear to have been derived from the carbonate itself and, ultimately, from the fluid from which they precipitated.

Several factors may contribute to development of positive Ce anomalies in the GSL ooids, e.g., strongly alkaline water conditions (Möller and Bau, 1993), and/or the presence of organic matter and Fe-Mn (oxyhydr)oxide fractions (Bau, 1999; Pourret et al., 2008). Strongly alkaline waters (e.g., Lake Van, Lake Abhé, and Venere lake, pH ≥ 9) may cause the formation of soluble tetravalent Ce-complexes rather than insoluble CeO_2, leading to distinct positive Ce anomalies in waters and associated carbonate sediments (Möller and Bau, 1993; Reimer et al., 2009; Dekov et al., 2014; Censi et al., 2015). Similar lake-water conditions may also occur in the GSL (pH = 8.6) (Domagalski et al., 1990), and affect the behavior of Ce in GSL ooids. On the other hand, we noted that with increasing Zr concentrations, (1) Eu and Gd anomalies are reduced in size but positive Ce anomalies are sustained, and (2) Fe concentrations increase strongly (Figs. 7D, and S5-E and -F). It is likely that some exogenous source of dissolved Ce liberated by Fe (oxyhydr)oxides, potentially in response to redox fluctuation (Sholkovitz et al., 1992; Bau et al., 1997). Continuous monitoring of shallow GSL waters shows that dissolved oxygen levels fluctuate rapidly, from a maximum during the day (to 40 mg/L) to a minimum at night (~0 mg/L), in response to diurnal cycles in photosynthetic activity and wind-induced vertical mixing (Wurtsbaugh et al., 2012). Such redox variations may mobilize excess Ce^{3+} from earlier-precipitated Fe (oxyhydr)oxides in lake-floor sediments, especially through dissolution at times of redox interface rise (de Baar et al., 1988; Ohta and Kawabe, 2001). Despite a fluctuating redox boundary, the major control on the generation of positive Ce anomalies within GSL ooid cortices may be related to strongly alkaline water conditions, and the influence from Fe-Mn (oxyhydr)oxide fractions remain uncertain and need to be further explored.

5.4. Ooid REE + Y compositions and their potential hydrochemical significance

5.4.1. Comparison of different analytical protocols

Comparison of analytical techniques (PFA to PFD) applied to different ooid components (bulk sands, carbonates and non-carbonates, and cortices) reveals their respective advantages for analysis of carbonate sediments. Strong acid digestions are useful for analysis of bulk sediments to determine the degree and type of siliciclastic influence on the trace-element chemistry of a bulk carbonate rock. Weak-acid digestions mainly sample the carbonate component of the sediment but still may release trace metals from the clay and organic colloid fractions and thus not truly represent the trace-element chemistry of the aqueous source (Nothdurft et al., 2004; Pourret et al., 2008; Bau et al., 2013). At the same time, these techniques may provide information about the compositions of specific siliciclastic contaminants (Tostevin et al., 2016). Laser ablation analyses are useful for targeting specific components even containing very similar mineral compositions (e.g., carbonate grains vs cements) (Della Porta et al., 2015; Li et al., 2017; Wallace et al., 2017; Hood et al., 2018) and allowing discrimination of more and less contaminated samples so that a contaminant mixing line can be constructed and the purest carbonate signature can be isolated. From this perspective, the LA-ICP-MS method would be better than the solution-based methods (including sequential leaching procedure) where admixtures of diagenetic carbonate, organic matter, and dust contamination may remain unresolved (Table 2).

Laser ablation of ooid cortices, although troubled by small

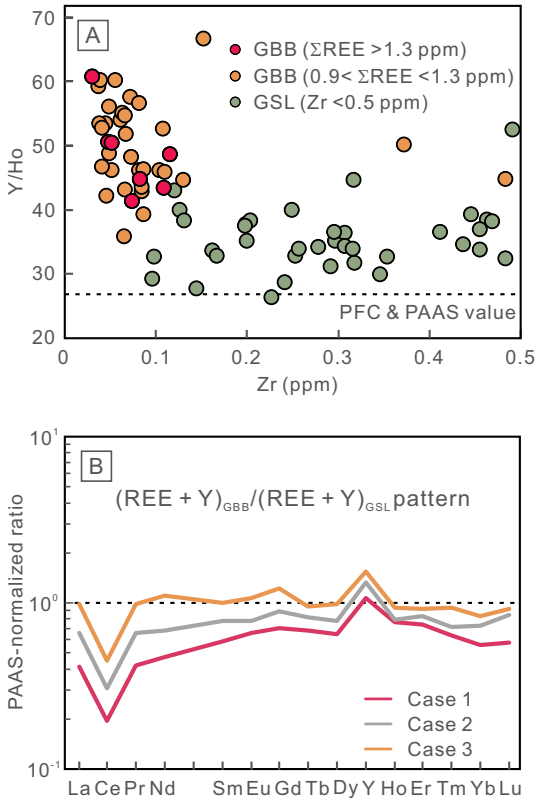

Fig. 8. (A) Zr versus Y/Ho for GBB (ΣREE > 0.9 ppm) and GSL (Zr < 0.5 ppm) ooid cortices from PFD. Note the lowermost value of Y/Ho in GSL is close to the result of the non-carbonate component obtained by PFC, which approaches the Y/Ho value of PAAS. (B) Ratios of GBB to GSL ooid cortical REE + Y compositions for different Zr and ΣREE values. Case 1: ooid cortices with ΣREE > 0.9 ppm at GBB (mean value), and ooid cortices with Zr < 0.5 ppm at GSL (mean value); Case 2: ooid cortices with ΣREE > 0.9 ppm at GBB (mean value), and least contaminated ooid cortex (Zr = 0.096) at GSL; Case 3: ooid cortices with ΣREE > 1.3 ppm at GBB (mean value), and least contaminated ooid cortex at GSL. See Section 5.4.2 for details.

analytical volumes and low elemental concentrations, can successfully yield aqueous REE + Y patterns and detailed information about small-scale compositional variation within individual ooids, as well as helping to identify specific contaminants and early diagenetic influences. Apart from a few outliers, Y/Ho ratios in reliable Bahamian ooids (i.e., ΣREE > 0.9 ppm) decrease rapidly from > 60 to ~40–50 as Zr approaches 0.1 ppm (Fig. 8A). The low-Zr ooids that yield the highest Y/Ho ratios (> 60) provide the most pristine hydrogenous signal. The higher-Zr ooids with Y/Ho values of ~40–50 conform to values seen in western Atlantic surface waters (42–52; Fig. S4-C and Table S5), implying a degree of contamination by siliciclastic and organic-matter REEs (respectively < 0.2% and < 0.5% as inferred from modeling) in actual surface seawater (Fig. 4H and I) (Osborne et al., 2015), possibly through trapping of colloidal phases or dissolved material in ooid cortices.

5.4.2. Significance of ooid REE + Y compositions in marine and lacustrine environments

Pure ooid grains developed in shallow-water, high-energy carbonate depositional settings can be a good target for investigating paleo-seawater REE compositions. Key advantages are (1) the relatively dense structure of ooid cortices, and their nearly pure carbonate composition within and between ooids from a given locale, (2) seawater-like porewater compositions in the shallow surface sediments of ooid shoals related to their high mobility and permeability, (3) easy identification and wide distribution of ooids in most of geological periods, and (4) an absence of biological fractionation effects, nearly uniform D_{ooid}, and relatively higher REE concentrations than in most bioclasts. In addition, minor contributions of terrigenous particles in ooid cortices can be detected and isolated through spot analyses and construction of a contaminant mixing model. The systematic evaluation of modern Bahamian ooids conducted in this study provides a solid frame for understanding the REE properties of paleo-marine systems (Fig. 6C).

For the mixed siliciclastic-carbonate environment of the GSL, the laser ablation method is useful in revealing differences in REE compositions between least-contaminated and typical ooid cortices which are interpreted to have a degree of siliciclastic contamination. Although ooid cortices with Zr contents > 0.5 ppm were excluded to avoid obvious siliciclastic contamination, there is still a clear positive relationship between Zr values and other metals (e.g., Al and Ti; Fig. 7D). The least-contaminated ooid cortex, defined by a low Zr concentration (0.096 ppm) and a robust REE + Y pattern, was selected in order to isolate the hydrogenous signal in the carbonate fraction (Fig. 7E). Siliciclastic contamination (shown by increasing Zr content) is linked to higher ΣREE concentrations and reduced LREE depletion in PAAS-normalized REE + Y distributions (Fig. 7E and F; cf. Kamber et al. (2004)). Furthermore, the REE + Y distribution of the least-contaminated GSL ooid is similar to those of reliable GBB ooid cortices. Consequently, comparing these two distributions as a ratio results in a relatively flat REE distribution pattern (except for Ce and Y) (Fig. 8B). If the GBB ooids with the highest ΣREE contents (> 1.3 ppm; mean 1.61 ± 0.39 ppm, $n = 7$; similar to that of the least-contaminated GSL ooid, 1.93 ppm) are used in the normalization, the ratio of $(REE + Y)_{GBB}/(REE + Y)_{GSL}$ is very close to 1.0 (i.e., 0.99 ± 0.10; Fig. 8B). Hence, the least-contaminated aragonite ooids from these two different depositional settings have almost uniform REE + Y distributions with the major exceptions of Ce and Y anomalies. Because similar alkalinity and pH conditions exist at GBB (alkalinity: 6.50 to 9.62 meq/L, pH: 8.55–8.75) (Diaz et al., 2015) and GSL (alkalinity: ~7 meq/L; pH: 8.6) (Domagalski et al., 1990; Jones et al., 2009; Chagas et al., 2016), we infer that the carbonate complexation system may be responsible for the observed uniformity of PAAS-normalized REE + Y distribution patterns between GBB and GSL.

6. Conclusions

Sample-digestion ICP-MS analysis of bulk ooid sands from Great Bahama Banks (GBB) shows a seawater-like REE + Y distribution characterized by LREE depletion, positive La, Gd, and Y anomalies, and a negative Ce anomaly. The ooid sands contain miniscule amounts of siliciclastic-dust-sourced REEs (< 0.2% of ΣREE), but admixture of this contaminant was sufficient to have a measurable effect on the LREE content of Joulter Cays ooids due to their low ΣREE concentrations. The most reliably measured ooid cortices (i.e., having ΣREE > 0.9 ppm) exhibit more uniform seawater-like REE + Y patterns that conform to the results from weak-acid-digestion ICP-MS analysis (PFB) and published REE compositions of Western Atlantic surface waters.

For Great Salt Lake (GSL) ooids, the different processing flows reveal that bulk-sample REE signatures represent a mixture of REEs from ooid cortex, carbonate and non-carbonate ooid nuclei, and siliciclastic contaminants. Illite clay particles within the cortices may have been partially digested in acetic acid and thus affected the LREE compositions yielded by PFB. Unlike GBB ooids, the nearly uniform positive Ce anomalies of GSL ooids imply strongly alkaline lake-water conditions. The strict exclusion of contaminant particles yields ooid cortical REE + Y patterns that are generally similar to those of reliable ooid cortices from the GBB. This counterintuitive result can be understood as the product of similar watermass alkalinity and pH at GBB and GSL. Nonetheless, Ce anomalies and Y/Ho ratios serve to distinguish lacustrine GSL ooids ($(Ce/Ce^*)_{SN} > 1$, Y/Ho < 40) from marine GBB ooids ($(Ce/Ce^*)_{SN} < 1$, Y/Ho > 40).

The use of multiple analytical protocols in this study provided insights into how best to analyze ooid REE + Y chemistry. First, laser-ablation analyses (PFD) yield results with unacceptably high uncertainties at low ΣREE concentrations (< 0.9 ppm), although even the low concentration data converge on a reasonable value provided they can be plotted along a trend of increasing concentration. Second, for bulk carbonates, miniscule amounts of siliciclastic-dust-sourced REEs (< 0.2% of ΣREE) were sufficient to have a measurable effect on LREE patterns due to low ΣREE concentrations. Third, even weak acid sample digestion procedures for impure carbonate rocks (e.g., single-step acetic acid leaching) may partially digest clay minerals (e.g., illite). These problems, which frequently arise in analysis of modern and ancient carbonates, need to be avoided when attempting to recover paleo-seawater REE + Y signatures. The results of this study demonstrate that ooids can potentially preserve the REE + Y composition of paleo-seawater, if suitable analytical methods are adopted and influences from siliciclastic contamination are excluded through appropriate screening of results. As ooids are abundant through much of Earth history and have distinctive morphologies allowing petrographic recognition of recrystallization and diagenetic alteration, they provide a good target for future studies aiming to reconstruct the evolution of seawater REE + Y chemistry through time.

Acknowledgments

We greatly appreciate the assistance of Drs. William Jones and Liyin Pan in collecting samples from Schooner Cays (Bahamas) and Antelope Island (Great Salt Lake), respectively. We are deeply greatful for the permission to visit the database of GEOTRACES publications. Graduate students Kai Zeng, Jiating Deng and Zhengqiang Che are thanked for their careful study on ooid microscopic features. Dr. Teresa Ubide is appreciated for Iolite training. We thank Dr. Ashleigh Hood and an anonymous reviewer, as well as the editor Prof. Balz Kamber for their constructive comments on an earlier version, which greatly improved the quality of this paper. This study was supported by the National Natural Science Foundation of China (41872119 and 41502115), the National Science and Technology Major Project (2016ZX05004002-001), the Key Laboratory of Carbonate Reservoirs, CNPC (RIPED-HZDZY-2018-JS-198 and 2018D-5006-35), and the IAS Post-Doctoral Research Grants (Spring Session, 2017).

Appendix A. Supplementary data

Supplementary data to this article can be found online at https://doi.org/10.1016/j.chemgeo.2019.01.015.

References

Abbott, A.N., Haley, B.A., McManus, J., Reimers, C.E., 2015. The sedimentary flux of dissolved rare earth elements to the ocean. Geochim. Cosmochim. Acta 154, 186–200.
Akagi, T., Hashimoto, Y., F-F, F., Tsuno, H., Tao, H., Nakano, Y., 2004. Variation of the distribution coefficients of rare earth elements in modern coral-lattices: species and site dependencies. Geochim. Cosmochim. Acta 68, 2265–2273.
Andres, M.S., Sumner, D.Y., Reid, R.P., Swart, P.K., 2006. Isotopic fingerprints of microbial respiration in aragonite from Bahamian stromatolites. Geology 34, 973.
Bau, M., 1999. Scavenging of dissolved yttrium and rare earths by precipitating iron oxyhydroxide: experimental evidence for Ce oxidation, Y-Ho fractionation, and lanthanide tetrad effect. Geochim. Cosmochim. Acta 63, 67–77.
Bau, M., Dulski, P., 1996. Distribution of yttrium and rare-earth elements in the Penge and Kuruman iron-formations, Transvaal Supergroup, South Africa. Precambrian Res. 79, 37–55.
Bau, M., Möller, P., Dulski, P., 1997. Yttrium and lanthanides in eastern Mediterranean seawater and their fractionation during redox-cycling. Mar. Chem. 56, 123–131.
Bau, M., Tepe, N., Mohwinkel, D., 2013. Siderophore-promoted transfer of rare earth elements and iron from volcanic ash into glacial meltwater, river and ocean water. Earth Planet. Sci. Lett. 364, 30–36.
Bayon, G., German, C.R., Boella, R.M., Milton, J.A., Taylor, R.N., Nesbitt, R.W., 2002. An improved method for extracting marine sediment fractions and its application to Sr and Nd isotopic analysis. Chem. Geol. 187, 179–199.
Bayon, G., German, C.R., Burton, K.W., Nesbitt, R.W., Rogers, N., 2004. Sedimentary Fe–Mn oxyhydroxides as paleoceanographic archives and the role of aeolian flux in regulating oceanic dissolved REE. Earth Planet. Sci. Lett. 224, 477–492.
Bayon, G., Toucanne, S., Skonieczny, C., André, L., Bermell, S., Cheron, S., Dennielou, B., Etoubleau, J., Freslon, N., Gauchery, T., Germain, Y., Jorry, S.J., Ménot, G., Monin, L., Ponzevera, E., Rouget, M.L., Tachikawa, K., Barrat, J.A., 2015. Rare earth elements and neodymium isotopes in world river sediments revisited. Geochim. Cosmochim. Acta 170, 17–38.
Bergman, K.L., Westphal, H., Janson, X., Poiriez, A., Eberli, G.P., 2010. Controlling parameters on facies geometries of the Bahamas, an isolated carbonate platform environment. In: Westphal, H., Riegl, B., Eberli, G.P. (Eds.), Carbonate Depositional Systems: Assessing Dimensions and Controlling Parameters: The Bahamas, Belize and the Persian/Arabian Gulf. Springer Netherlands, Dordrecht, pp. 5–80.
Byrne, R.H., Kim, K.-H., 1990. Rare earth element scavenging in seawater. Geochim. Cosmochim. Acta 54, 2645–2656.
Censi, P., Cangemi, M., Brusca, L., Madonia, P., Saiano, F., Zuddas, P., 2015. The behavior of rare-earth elements, Zr and Hf during biologically-mediated deposition of silica-stromatolites and carbonate-rich microbial mats. Gondwana Res. 27, 209–215.
Chagas, A.A.P., Webb, G.E., Burne, R.V., Southam, G., 2016. Modern lacustrine microbialites: towards a synthesis of aqueous and carbonate geochemistry and mineralogy. Earth-Sci. Rev. 162, 338–363.
Chen, J.B., Algeo, T.J., Zhao, L.S., Chen, Z.Q., Cao, L., Zhang, L., Li, Y., 2015. Diagenetic uptake of rare earth elements by bioapatite, with an example from Lower Triassic conodonts of South China. Earth-Sci. Rev. 149, 181–202.
Chen, L., Liu, Y.S., Hu, Z.C., Gao, S., Zong, K.Q., Chen, H.H., 2011. Accurate determinations of fifty-four major and trace elements in carbonate by LA-ICP-MS using normalization strategy of bulk components as 100%. Chem. Geol. 284, 283–295.
Chester, R., Hughes, M.J., 1967. A chemical technique for the separation of ferro-manganese minerals, carbonate minerals and adsorbed trace elements from pelagic sediments. Chem. Geol. 2, 249–262.
de Baar, H.J., German, C.R., Elderfield, H., van Gaans, P., 1988. Rare earth element distributions in anoxic waters of the Cariaco Trench. Geochim. Cosmochim. Acta 52, 1203–1219.
de Baar, H.J.W., Bacon, M.P., Brewer, P.G., Bruland, K.W., 1985. Rare earth elements in the Pacific and Atlantic Oceans. Geochim. Cosmochim. Acta 49, 1943–1959.
de Paula-Santos, G.M., Caetano-Filho, S., Babinski, M., Enzweiler, J., 2018. Rare earth elements of carbonate rocks from the Bambuí Group, southern São Francisco Basin, Brazil, and their significance as paleoenvironmental proxies. Precambrian Res. 305, 327–340.
Dekov, V.M., Egueh, N.M., Kamenov, G.D., Bayon, G., Lalonde, S.V., Schmidt, M., Liebetrau, V., Munnik, F., Fouquet, Y., Tanimizu, M., Awaleh, M.O., Guirreh, I., Le Gall, B., 2014. Hydrothermal carbonate chimneys from a continental rift (Afar Rift): mineralogy, geochemistry, and mode of formation. Chem. Geol. 387, 87–100.
Della Porta, G., Webb, G.E., McDonald, I., 2015. REE patterns of microbial carbonate and cements from Sinemurian (Lower Jurassic) siliceous sponge mounds (Djebel Bou Dahar, High Atlas, Morocco). Chem. Geol. 400, 65–86.
Diaz, M.R., Swart, P.K., Eberli, G.P., Oehlert, A.M., Devlin, Q., Saeid, A., Altabet, M.A., 2015. Geochemical evidence of microbial activity within ooids. Sedimentology 62, 2090–2112.
Domagalski, J.L., Eugster, H.P., Jones, B.F., 1990. Trace metal geochemistry of Walker, Mono, and Great Salt Lakes. In: Spencer, R.J., Chou, I.-M. (Eds.), Fluid-Mineral Interactions: A Tribute to H. P. Eugster. No. 2. The Geochemical Society, Special Publication, Washington, DC, pp. 315–335.
Elderfield, H., Greaves, M.J., 1982. The rare earth elements in seawater. Nature 296, 214–219.
Elderfield, H., Sholkovitz, E.R., 1987. Rare earth elements in the pore waters of reducing nearshore sediments. Earth Planet. Sci. Lett. 82, 280–288.
Elderfield, H., Upstill-Goddard, R., Sholkovitz, E.R., 1990. The rare earth elements in rivers, estuaries, and coastal seas and their significance to the composition of ocean waters. Geochim. Cosmochim. Acta 54, 971–991.
Flügel, E., 2004. Microfacies of Carbonate Rocks: Analysis, Interpretation and Application. Springer-Verlag, Berlin Heidelberg.
Freslon, N., Bayon, G., Toucanne, S., Bermell, S., Bollinger, C., Chéron, S., Etoubleau, J., Germain, Y., Khripounoff, A., Ponzevera, E., Rouget, M.-L., 2014. Rare earth elements and neodymium isotopes in sedimentary organic matter. Geochim. Cosmochim. Acta 140, 177–198.
German, C.R., Elderfield, H., 1990. Application of the Ce anomaly as a paleoredox indicator: the ground rules. Paleoceanography 5, 823–833.
Goldstein, S.J., Jacobsen, S.B., 1988. Rare earth elements in river waters. Earth Planet. Sci. Lett. 89, 35–47.
Haley, B.A., Klinkhammer, G.P., McManus, J., 2004. Rare earth elements in pore waters of marine sediments. Geochim. Cosmochim. Acta 68, 1265–1279.
Haley, B.A., Klinkhammer, G.P., Mix, A.C., 2005. Revisiting the rare earth elements in foraminiferal tests. Earth Planet. Sci. Lett. 239, 79–97.
Halley, R.B., 1977. Ooid fabric and fracture in the Great Salt Lake and the geologic record. J. Sediment. Res. 47, 1099–1120.
Henderson, P., 1984. Rare Earth Element Geochemistry. Elsevier Science Publisher, Amsterdam.
Hood, A.v.S., Planavsky, N.J., Wallace, M.W., Wang, X.L., 2018. The effects of diagenesis on geochemical paleoredox proxies in sedimentary carbonates. Geochim. Cosmochim. Acta 232, 265–287.
Jones, B.F., Naftz, D.L., Spencer, R.J., Oviatt, C.G., 2009. Geochemical evolution of Great Salt Lake, Utah, USA. Aquat. Geochem. 15, 95–121.
Kalvoda, J., Kumpan, T., Hola, M., Babek, O., Kanicky, V., Skoda, R., 2018. Fine-scale LA-ICP-MS study of redox oscillations and REEY cycling during the latest Devonian Hangenberg Crisis (Moravian Karst, Czech Republic). Palaeogeogr. Palaeoclimatol. Palaeoecol. 493, 30–43.

Kamber, B.S., Bolhar, R., Webb, G.E., 2004. Geochemistry of late Archaean stromatolites from Zimbabwe: evidence for microbial life in restricted epicontinental seas. Precambrian Res. 132, 379–399.
Lawrence, M.G., Greig, A., Collerson, K.D., Kamber, B.S., 2006. Rare earth element and yttrium variability in South East Queensland waterways. Aquat. Geochem. 12, 39–72.
Lawrence, M.G., Kamber, B.S., 2006. The behaviour of the rare earth elements during estuarine mixing—revisited. Mar. Chem. 100, 147–161.
Li, F., Yan, J.X., Burne, R.V., Chen, Z.-Q., Algeo, T.J., Zhang, W., Tian, L., Gan, Y.L., Liu, K., Xie, S., 2017. Paleo-seawater REE compositions and microbial signatures preserved in laminae of Lower Triassic ooids. Palaeogeogr. Palaeoclimatol. Palaeoecol. 486, 96–107.
Liu, Y.S., Hu, Z.C., Gao, S., Günther, D., Xu, J., Gao, C.G., Chen, H.H., 2008. In situ analysis of major and trace elements of anhydrous minerals by LA-ICP-MS without applying an internal standard. Chem. Geol. 257, 34–43.
McLennan, S.M., 1989. Rare earth elements in sedimentary rocks: influence of provenance and sedimentary processes. In: Lipin, B.R., Mckay, G.A. (Eds.), Geochemistry and Mineralogy of Rare Earth Elements. 21, Reviews in Mineralogy, pp. 169–200.
Meredith, E.O., 1961. Separation of clay minerals from carbonate rocks by using acid. J. Sediment. Res. 31, 123–129.
Moffett, J.W., 1990. Microbially mediated cerium oxidation in sea water. Nature 345, 421–423.
Möller, P., Bau, M., 1993. Rare-earth patterns with positive cerium anomaly in alkaline waters from Lake Van, Turkey. Earth Planet. Sci. Lett. 117, 671–676.
Nothdurft, L.D., Webb, G.E., Kamber, B.S., 2004. Rare earth element geochemistry of Late Devonian reefal carbonates, Canning Basin, Western Australia: confirmation of a seawater REE proxy in ancient limestones. Geochim. Cosmochim. Acta 68, 263–283.
Nozaki, Y., 2001. Rare earth elements and their isotopes in the ocean. In: Steele, J.H., Thorpe, S.A., Turekian, K.K. (Eds.), Encyclopedia of Ocean Sciences. Academic Press, Oxford, pp. 2354–2366.
Nozaki, Y., Zhang, J., Amakawa, H., 1997. The fractionation between Y and Ho in the marine environment. Earth Planet. Sci. Lett. 148, 329–340.
Ohta, A., Kawabe, I., 2001. REE (III) adsorption onto Mn dioxide (δ-MnO_2) and Fe oxyhydroxide: Ce (III) oxidation by δ-MnO_2. Geochim. Cosmochim. Acta 65, 695–703.
Osborne, A.H., Haley, B.A., Hathorne, E.C., Plancherel, Y., Frank, M., 2015. Rare earth element distribution in Caribbean seawater: continental inputs versus lateral transport of distinct REE compositions in subsurface water masses. Mar. Chem. 177, 172–183.
Osborne, A.H., Hathorne, E.C., Schijf, J., Plancherel, Y., Böning, P., Frank, M., 2017. The potential of sedimentary foraminiferal rare earth element patterns to trace water masses in the past. Geochem. Geophys. Geosyst. 18, 1550–1568.
Palmer, M.R., 1985. Rare earth elements in foraminifera tests. Earth Planet. Sci. Lett. 73, 285–298.
Paton, C., Hellstrom, J., Paul, B., Woodhead, J., Hergt, J., 2011. Iolite: freeware for the visualisation and processing of mass spectrometric data. J. Anal. At. Spectrom. 26, 2508–2518.
Piper, D.Z., 1974. Rare earth elements in the sedimentary cycle: a summary. Chem. Geol. 14, 285–304.
Ponnurangam, A., Bau, M., Brenner, M., Koschinsky, A., 2016. Mussel shells of *Mytilus edulis* as bioarchives of the distribution of rare earth elements and yttrium in seawater and the potential impact of pH and temperature on their partitioning behavior. Biogeosciences 13, 751–760.
Pourmand, A., Prospero, J.M., Sharifi, A., 2014. Geochemical fingerprinting of trans-Atlantic African dust based on radiogenic Sr-Nd-Hf isotopes and rare earth element anomalies. Geology 42, 675–678.
Pourret, O., Davranche, M., Gruau, G., Dia, A., 2008. New insights into cerium anomalies in organic-rich alkaline waters. Chem. Geol. 251, 120–127.
Reid, R.P., Macintyre, I.G., 2000. Microboring versus recrystallization: further insight into the micritization process. J. Sediment. Res. 70, 24–28.
Reijmer, J.J.G., Swart, P.K., Bauch, T., Otto, R., Reuning, L., Roth, S., Zechel, S., 2001. A re-evaluation of facies on Great Bahama Bank I: new facies maps of Western Great Bahama Bank. In: Swart, P.K., Eberli, G.P., Mckenzie, J.A., Jarvis, I., Stevens, T. (Eds.), Perspectives in Carbonate Geology. IAS Special Publication. No. 41. Wiley-Blackwell, Oxford, pp. 29–46.
Reimer, A., Landmann, G., Kempe, S., 2009. Lake Van, eastern Anatolia, hydrochemistry and history. Aquat. Geochem. 15, 195–222.
Saha, N., Webb, G.E., Zhao, J.X., 2016. Coral skeletal geochemistry as a monitor of inshore water quality. Sci. Total Environ. 566–567, 652–684.
Scherer, M., Seitz, H., 1980. Rare-earth element distribution in Holocene and Pleistocene corals and their redistribution during diagenesis. Chem. Geol. 28, 279–289.
Schlitzer, R., Anderson, R.F., Dodas, E.M., Lohan, M., Geibere, W., Tagliabue, A., ... Zurbrick, C., 2018. The GEOTRACES Intermediate Data Product 2017. Chem. Geol. 493, 210–223.
Shields, G., Stille, P., 2001. Diagenetic constraints on the use of cerium anomalies as palaeoseawater redox proxies: an isotopic and REE study of Cambrian phosphorites. Chem. Geol. 175, 29–48.
Shields, G.A., Webb, G.E., 2004. Has the REE composition of seawater changed over geological time? Chem. Geol. 204, 103–107.
Shiller, A.M., 2002. Seasonality of dissolved rare earth elements in the lower Mississippi River. Geochem. Geophys. Geosyst. 3, 1068.
Sholkovitz, E., Shen, G.T., 1995. The incorporation of rare earth elements in modern coral. Geochim. Cosmochim. Acta 59, 2749–2756.
Sholkovitz, E.R., Landing, W.M., Lewis, B.L., 1994. Ocean particle chemistry: the fractionation of rare earth elements between suspended particles and seawater. Geochim. Cosmochim. Acta 58, 1567–1579.
Sholkovitz, E.R., Shaw, T.J., Schneider, D.L., 1992. The geochemistry of rare earth elements in the seasonally anoxic water column and porewaters of Chesapeake Bay. Geochim. Cosmochim. Acta 56, 3389–3402.
Siahi, M., Hofmann, A., Master, S., Mueller, C.W., Gerdes, A., 2017. Carbonate ooids of the Mesoarchaean Pongola Supergroup, South Africa. Geobiology 15, 750–766.
Song, Y.-H., Choi, M.S., 2009. REE geochemistry of fine-grained sediments from major rivers around the Yellow Sea. Chem. Geol. 266, 328–342.
Spencer, R.J., Baedecker, M.J., Eugster, H.P., Forester, R.M., Goldhaber, M.B., Jones, B.F., Kelts, K., McKenzie, J., Madsen, D.B., Rettig, S.L., Rubin, M., Bowser, C.J., 1984. Great Salt Lake, and precursors, Utah: the last 30,000 years. Contrib. Mineral. Petrol. 86, 321–334.
Swart, P.K., Oehlert, A.M., Mackenzie, G.J., Eberli, G.P., Reijmer, J.J.G., 2014. The fertilization of the Bahamas by Saharan dust: a trigger for carbonate precipitation? Geology 42, 671–674.
Tanaka, K., Kawabe, I., 2006. REE abundances in ancient seawater inferred from marine limestone and experimental REE partition coefficients between calcite and aqueous solution. Geochem. J. 40, 425–435.
Tostevin, R., Shields, G.A., Tarbuck, G.M., He, T., Clarkson, M.O., Wood, R.A., 2016. Effective use of cerium anomalies as a redox proxy in carbonate-dominated marine settings. Chem. Geol. 438, 146–162.
Ulrich, T., Kamber, B.S., Jugo, P.J., Tinkham, D.K., 2009. Imaging element-distribution patterns in minerals by laser ablation - inductively coupled plasma - mass spectrometry (La-ICP-MS). Can. Mineral. 47, 1001–1012.
van de Flierdt, T., Pahnke, K., Amakawa, H., Andersson, P., Basak, C., Coles, B., Colin, C., Crocket, K., Frank, M., Frank, N., Goldstein, S.L., Goswami, V., Haley, B.A., Hathorne, E.C., Hemming, S.R., Henderson, G.M., Jeandel, C., Jones, K., Kreissig, K., Lacan, F., Lambelet, M., Martin, E.E., Newkirk, D.R., Obata, H., Pena, L., Piotrowski, A.M., Pradoux, C., Scher, H.D., Schöberg, H., Singh, S.K., Stichel, T., Tazoe, H., Vance, D., Yang, J., 2012. GEOTRACES intercalibration of neodymium isotopes and rare earth element concentrations in seawater and suspended particles. Part 1: reproducibility of results for the international intercomparison. Limnol. Oceanogr. Methods 10, 234–251.
Wallace, M.W., Hood, A.v.S., Shuster, A., Greig, A., Planavsky, N.J., Reed, C.P., 2017. Oxygenation history of the Neoproterozoic to early Phanerozoic and the rise of land plants. Earth Planet. Sci. Lett. 466, 12–19.
Webb, G.E., Kamber, B.S., 2000. Rare earth elements in Holocene reefal microbialites: a new shallow seawater proxy. Geochim. Cosmochim. Acta 64, 1557–1565.
Webb, G.E., Kamber, B.S., 2011. Trace element geochemistry as a tool for interpreting microbialites. In: Golding, S.D., Glikson, M. (Eds.), Earliest Life on Earth: Habitats, Environments and Methods of Detection. Springer, Dordrecht, pp. 127–170.
Wurtsbaugh, W.A., Marcarelli, A.M., Boyer, G.L., 2012. Eutrophication and Metal Concentrations in Three Bays of the Great Salt Lake (USA). Watershed Sciences Faculty Publications. Paper 550.
Zaky, A.H., Azmy, K., Brand, U., Svavarsson, J., 2016a. Rare earth elements in deep-water articulated brachiopods: an evaluation of seawater mass. Chem. Geol. 435, 22–34.
Zaky, A.H., Brand, U., Azmy, K., Logan, A., Hooper, R.G., Svavarsson, J., 2016b. Rare earth elements of shallow-water articulated brachiopods: a bathymetric sensor. Palaeogeogr. Palaeoclimatol. Palaeoecol. 461, 178–194.
Zhang, S., Henehan, M.J., Hull, P.M., Reid, R.P., Hardisty, D.S., Hood, A.v.S., Planavsky, N.J., 2017. Investigating controls on boron isotope ratios in shallow marine carbonates. Earth Planet. Sci. Lett. 458, 380–393.
Zhong, S., Mucci, A., 1995. Partitioning of rare earth elements (REEs) between calcite and seawater solutions at 25 °C and 1 atm, and high dissolved REE concentrations. Geochim. Cosmochim. Acta 59, 443–453.